Thin-airfoil aerodynamics in a rarefied gas wind tunnel: A theoretical study ⊘

R. Shapiro [ID] ; A. Manela ✉ [ID]

Check for updates

View Online   Export Citation
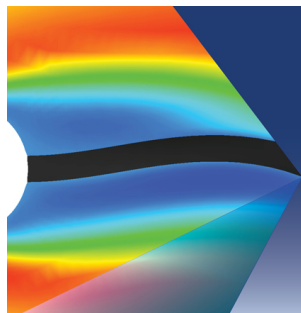
Physics of Fluids

Special Topic:

Fluid-Structure Interaction

Guest Editors: A-Man Zhang, Tiegang Liu, Boo Cheong Khoo and Nhan Phan-Thien

Submit Today!

AIP Publishing

AIP Publishing

Thin-airfoil aerodynamics in a rarefied gas wind tunnel: A theoretical study

View Online   Export Citation   CrossMark

R. Shapiro (iD) and A. Manela[a] (iD)

AFFILIATIONS

Faculty of Aerospace Engineering, Technion-Israel Institute of Technology, Haifa 32000, Israel

[a]Author to whom correspondence should be addressed: amanela@technion.ac.il

ABSTRACT

We study the steady aerodynamic field and loadings about a thin flat plate placed in a wind tunnel under non-continuum conditions. Considering a two-dimensional straight tunnel configuration, the flow is driven by either density or temperature differences between the inlet and outlet tunnel reservoirs, producing a pressure gradient across the channel. Focusing on highly rarefied conditions, we derive a semi-analytic description for the gas flow field in the free-molecular limit for diffuse- and specular-wall configurations. The solution is valid at arbitrary differences between the inlet and outlet reservoirs as well as plate angles of attack α. The results are compared with direct simulation Monte Carlo calculations, indicating that the free-molecular description is valid through $O(1)$ plate-size-based Knudsen numbers. The aerodynamic lift and drag forces are evaluated and their variations with α, reservoir conditions, and tunnel size are analyzed. At a fixed pressure ratio between the outlet and inlet reservoirs, the density-driven flow generates higher aerodynamic loads compared with its counterpart temperature-driven configuration, in line with the associated larger mass flow rate in the former. The results are discussed in light of the existing rarefied-gas description of the free-stream (non-confined) problem.

I. INTRODUCTION

Wind tunnels are ubiquitously used for investigating the interaction between aerodynamic structures and flowing air, yielding a measure for the aerodynamic performance of flying vehicles. Different from free-stream (FS) flight, the tunnel walls, as well as its open entrance and exit conditions, affect the flow field and consequent loadings. To mimic realistic flight conditions, these effects must, therefore, be evaluated and reduced. Glauert[1] was among the first to provide a systematic survey on tunnel interference on wings and airscrews, comparing experimental results and theoretical predictions and tabulating respective correction formulas. Further investigations have been carried out to extend Glauert's work, which is still accepted as a standard means for the estimation of wind tunnel corrections at low speeds.

To date, theoretical wind tunnel analyses have been limited to the continuum flow regime. However, at states where continuum conditions do not prevail, these analyses cannot be followed to predict the correct aerodynamic behavior. Such conditions take place at high stratospheric[2,3] and outer space[4–6] flights, which are of practical relevance, as well as in gas flows in microscale propulsion systems.[7–9] These span a large variety of flow velocities, ranging from subsonic to supersonic speeds. In particular, low-speed aerodynamics are

encountered in various space-flight applications, including landing on rarefied-atmosphere planets, where typical landing velocities are of the order of few meters per second and below.[10] Additionally, missions involving orbits surrounding asteroids and comets, whose mass is small, require flight velocities on the order of few meters per second about the encircled objects.[11] Since the realization of real-time flight experiments is overwhelmingly costly, the significance of conducting non-continuum wind tunnel measurements is evident. Several efforts have already been documented in the literature,[12–16] which, nevertheless, may clearly benefit from ever-more cost-effective theoretical investigations.

Rarefied gas aerodynamics has been studied since the 1950s, analyzing airfoils aerodynamic performance at free-stream conditions. To this end, Stadler and Zurick[17] investigated the free-molecular (FM) loading on several aerodynamic configurations. Focusing on a flat-plate geometry, more works followed, examining the effect of surface conditions,[18] gas rarefaction rates,[19–22] and thermal wall properties[23] on the structure aerodynamic properties. Additional studies have considered other NACA airfoil configurations, investigating their surrounding free-stream flow properties.[24–26] Most of these works rely on heavy-load numerical calculations, including the direct simulation

Monte Carlo (DSMC) method, model presentations of the Boltzmann equation, or continuum-limit-based CFD solvers. To the best of our knowledge, a counterpart theoretical study on the effect of tunnel confinement on rarefied gas aerodynamics is lacking.

In view of the above, the present work investigates the aerodynamic properties of a flat plate set in a two-dimensional wind tunnel at large Knudsen numbers. Focusing on highly rarefied flow conditions, semi-analytical predictions are obtained for the effects of channel walls on free-molecular aerodynamic loadings. A detailed study on the impact of channel inlet and outlet states, plate angle of attack, and surface boundary conditions is carried out. Different from traditional continuum-limit calculations, the present scheme remains valid at arbitrarily large angles of plate incidence and inlet-to-outlet ratios of channel conditions. The effect of surface reflections, varying between specular and diffuse wall emissions, is examined. The free-molecular results are validated through comparison with DSMC computations, to test the breakdown of the collisionless description with decreasing Knudsen numbers. The convergence of the obtained results to the free-stream description is discussed.

In Sec. II, the problem is stated. The free-molecular limit is analyzed in Sec. III, including both diffuse- and specular-wall solutions. The numerical DSMC scheme is described in Sec. IV, followed by our results and concluding comments in Secs. V and VI, respectively. Technical details are relegated to the appendices.

II. STATEMENT OF THE PROBLEM

A schematic of the problem is shown in Fig. 1. Consider a thin flat plate of chord c^* placed in a two-dimensional straight channel of total length L^* and width H^* (hereafter, asterisks denote dimensional quantities). The plate is fixed at an angle α to the negative x^*-axis in the clockwise direction, with its midchord origin point placed in the x^* and y^* middle points of the channel. It is assumed that the inlet and outlet channel sections are connected to equilibrium-set reservoirs, where a perfect monatomic gas is maintained at thermodynamic $(\rho_{\text{in}}^*, T_{\text{in}}^*)$ and $(\rho_{\text{out}}^*, T_{\text{out}}^*)$ equilibrium densities and temperatures,
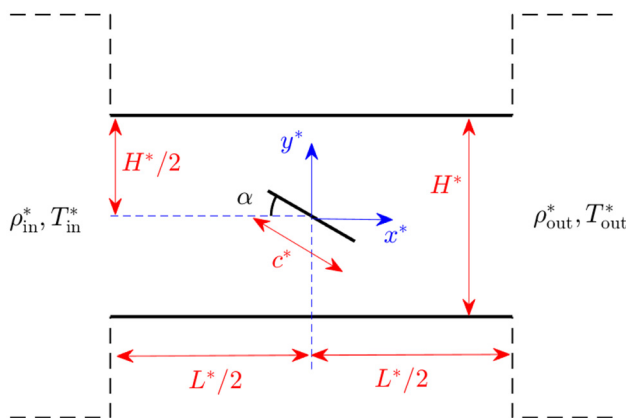
FIG. 1. Schematic of the problem: a thin flat plate of chord c^* is set in a two-dimensional straight channel of total length L^* and width H^*. The channel inlet and outlet sections are connected to equilibrium reservoirs set at densities ρ_{in}^* and ρ_{out}^*, and temperatures T_{in}^* and T_{out}^*, respectively. The plate is fixed at an angle α measured in the clockwise direction to the negative x^*-axis, with its midchord placed in the x^* and y^* middle points of the channel.

respectively. These correspond to equilibrium pressures $p_{\text{in}}^* = \rho_{\text{in}}^* \mathcal{R}^* T_{\text{in}}^*$ and $p_{\text{out}}^* = \rho_{\text{out}}^* \mathcal{R}^* T_{\text{out}}^*$ at the reservoirs, respectively, where $\mathcal{R}^*$ marks the specific gas constant. Gas particles entering the channel through the inlet and outlet sections are distributed according to the equilibrium Maxwellian distributions

$$f_{\text{in}}^*(\boldsymbol{\xi}^* \cdot \hat{\mathbf{x}} > 0) = \frac{\rho_{\text{in}}^*}{\pi^{3/2} U_{\text{mp}_{\text{in}}}^{*3}} \exp\left[-\frac{\xi^{*2}}{U_{\text{mp}_{\text{in}}}^{*2}}\right] \quad \text{and}$$

$$f_{\text{out}}^*(\boldsymbol{\xi}^* \cdot \hat{\mathbf{x}} < 0) = \frac{\rho_{\text{out}}^*}{\pi^{3/2} U_{\text{mp}_{\text{out}}}^{*3}} \exp\left[-\frac{\xi^{*2}}{U_{\text{mp}_{\text{out}}}^{*2}}\right], \tag{1}$$

where $U_{\text{mp}_{\text{in}}}^* = \sqrt{2\mathcal{R}^* T_{\text{in}}^*}$ and $U_{\text{mp}_{\text{out}}}^* = \sqrt{2\mathcal{R}^* T_{\text{out}}^*}$ denote the gas molecular most probable speeds at the inlet and outlet reservoirs, respectively. Additionally, $\boldsymbol{\xi}^* = (\xi_x^*, \xi_y^*, \xi_z^*)$ symbols the vector of molecular velocities, and $\hat{\mathbf{x}}$ is a unit vector in the positive x^*-direction. Strictly, Eq. (1) should be valid only at free molecular conditions, whereas end-effect corrections need to be taken into account at finite Knudsen numbers. This has been carried out in previous studies on rarefied gas channel flows (see, e.g., Ref. 27), where the correction has been interpreted in an effective amendment to the channel length. Nevertheless, since we examine highly rarefied flow conditions and focus primarily on the free-molecular regime, the expected impact of reservoir collisions is minor and Eq. (1) is applied throughout as a valid approximation. Gas-surface interactions of the gas particles with the plate and channel boundaries are modeled via the Maxwell boundary condition,[28]

$$f(\mathbf{r}_b^*, \boldsymbol{\xi}^* \cdot \hat{\mathbf{n}} > 0) = \beta \frac{\rho_b^*(\mathbf{r}_b^*)}{\pi^{3/2} U_{\text{mp}_b}^{*3}} \exp\left[-\frac{\xi^{*2}}{U_{\text{mp}_b}^{*2}}\right]$$
$$+ (1-\beta) f(\mathbf{r}_b^*, \boldsymbol{\xi}^* - 2(\boldsymbol{\xi}^* \cdot \hat{\mathbf{n}})\hat{\mathbf{n}}), \tag{2}$$

where the relative β and $(1-\beta)$ parts of the gas molecules are emitted diffusely and specularly, respectively, at each $\mathbf{r}_b^* = (x_b^*, y_b^*)$ location along the boundaries. Here, $\hat{\mathbf{n}}$ denotes a unit normal-to-surface vector directed into the gas, $\rho_b^*(\mathbf{r}_b^*)$ is a yet unknown function associated with the mass flux of particles emitted from the boundary, and $U_{\text{mp}_b}^* = \sqrt{2\mathcal{R}^* T_b^*}$ is the molecular most probable speed based on the boundary temperature T_b^*. The channel solid boundaries are assumed isothermal and are kept with the common inlet reservoir temperature $T_b^* = T_{\text{in}}^*$. Consideration of different wall temperatures, as studied in Ref. 23, may be readily applied, but is not followed here.

To render the problem dimensionless, we scale the position by the plate chord size c^*, the velocity by $U_{\text{mp}_{\text{in}}}^*$, and the density and temperature by ρ_{in}^* and T_{in}^*, respectively. The system description is then governed by the channel and airfoil reduced geometrical measures,

$$L = L^*/c^*, \quad H = H^*/c^* \text{ and } \alpha, \tag{3}$$

denoting the channel scaled length and width, together with the plate angle of attack, respectively. Additionally,

$$\rho_{\text{out}} \quad \text{and} \quad T_{\text{out}} \tag{4}$$

mark the scaled gas density and temperature at the outlet reservoir, respectively.

In what follows, we study the steady flow field in the tunnel at non-continuum conditions, focusing on the limit of high rarefaction

rates. We start by analyzing the free-molecular limit of the problem. The analytical results are then compared with DSMC predictions, to validate the ballistic description, test the breakdown of the free-molecular regime, and assess the effect of molecular collisions on the aerodynamic loads. No restrictions are made for the values of α, ρ_{out}, and T_{out}, which allow the analysis of the aerodynamic problem at arbitrarily large angles of attack as well as arbitrary pressure differences between the channel inlet and outlet reservoirs.

III. FREE-MOLECULAR LIMIT

Free-molecular conditions should prevail wherever the mean free path λ^* of a gas molecule is large compared to the problem characteristic length scale c^*. In a non-dimensional formulation, this requires that the Knudsen number,

$$\text{Kn} = \lambda^*/c^*, \tag{5}$$

be exceedingly large. For the steady two-dimensional setup considered, the gas state is governed by the probability density function $f = f(\mathbf{r}, \boldsymbol{\xi})$ of finding a gas molecule with position and velocity about $\mathbf{r} = (x, y)$ and $\boldsymbol{\xi} = (\xi_x, \xi_y, \xi_z)$, respectively. While the hydrodynamic (macroscopic) gas motion is confined to the (x, y) plane, molecular gas movements are distributed in all spatial directions. At free-molecular ($\text{Kn} \to \infty$) conditions, $f(\mathbf{r}, \boldsymbol{\xi})$ satisfies the collisionless two-dimensional ($\mathbf{r}$-dependent) Boltzmann equation,[29]

$$\xi_x \frac{\partial f}{\partial x} + \xi_y \frac{\partial f}{\partial y} = 0. \tag{6}$$

The equation is supplemented by the scaled form of the Maxwell boundary condition [see Eq. (2)],

$$f(\mathbf{r}_b, \boldsymbol{\xi} \cdot \hat{\mathbf{n}} > 0) = \beta \frac{\rho_b(\mathbf{r}_b)}{\pi^{3/2}} \exp\left[-\xi^2\right] + (1-\beta) f(\mathbf{r}_b, \boldsymbol{\xi} - 2(\boldsymbol{\xi} \cdot \hat{\mathbf{n}})\hat{\mathbf{n}}), \tag{7}$$

assigned to the reflected particles at each solid surface, combined with the non-dimensional counterpart of Eq. (1),

$$f_{\text{in}} = f(x = -L/2, -H/2 \leq y \leq H/2, \xi_x > 0) = \frac{1}{\pi^{3/2}} \exp\left[-\xi^2\right] \text{ and}$$

$$f_{\text{out}} = f(x = L/2, -H/2 \leq y \leq H/2, \xi_x < 0) = \frac{\rho_{\text{out}}}{\pi^{3/2} T_{\text{out}}^{3/2}} \exp\left[-\frac{\xi^2}{T_{\text{out}}}\right], \tag{8}$$

prescribing the state of incoming particles at the inlet and outlet sections, respectively. The problem formulated in Eqs. (6)–(8) is analyzed separately for the cases of fully diffuse ($\beta = 1$; Sec. III A) and fully specular ($\beta = 0$; Sec. III B) walls. These two setups may be considered as limit realizations of completely accommodating and reflecting boundaries, respectively. Diffuse scattering takes place over "rough" surfaces, where the colliding particles attain thermal equilibrium with the reflecting wall and evaporate accordingly. Specular interactions occur when the incident molecules collide with a solid surface and rebound elastically as if hitting a perfectly smooth wall. While none of these idealized scenarios appears to exist in reality, it is commonly accepted that wall reflections from "engineering" surfaces may be described, in a variety of applications, as a combination of diffuse and specular interactions, as formulated in Eq. (7). The combined diffuse–specular

($0 < \beta < 1$) case then composes the two limits and is therefore not considered hereafter in detail.

A. Diffuse reflecting walls

Setting $\beta = 1$ in Eq. (7), the state of each gas particle in the tunnel is determined by its last reflection from the free or solid-wall boundaries. The general solution for the problem is consequently given by

$$f(\mathbf{r}, \boldsymbol{\xi}) = \frac{\widetilde{\rho}(\mathbf{r}, \boldsymbol{\xi})}{\pi^{3/2} \widetilde{T}^{3/2}} \exp\left[-\frac{\xi^2}{\widetilde{T}}\right], \tag{9}$$

where $\widetilde{T}$ is the prescribed temperature of the emitting boundary and $\widetilde{\rho}(x, y, \mathbf{c})$ is an unknown function to be determined hereby. Given a particle position (x, y) and its in-plane velocity vector (ξ_x, ξ_y), the identity of its recent emitting surface is known uniquely.

Calculation of $\widetilde{\rho}(x, y, \mathbf{c})$ is carried out by imposing the impermeability condition,

$$\int_{\boldsymbol{\xi} \cdot \hat{\mathbf{n}} > 0} (\boldsymbol{\xi} \cdot \hat{\mathbf{n}}) f(\mathbf{r}_b, \boldsymbol{\xi}) \text{d}\boldsymbol{\xi} + \int_{\boldsymbol{\xi} \cdot \hat{\mathbf{n}} < 0} (\boldsymbol{\xi} \cdot \hat{\mathbf{n}}) f(\mathbf{r}_b, \boldsymbol{\xi}) \text{d}\boldsymbol{\xi} = 0, \tag{10}$$

along each side of the plate and the channel solid walls. Here, the first and second integrals express the separate contributions of the outgoing and incoming particles to the macroscopic gas velocity normal to the surface, respectively. At a given location, incoming particles may arrive from different channel boundaries, and their respective contributions should be accordingly accounted for.

We demonstrate the derivation of the walls' impermeability condition by detailing its calculation at the upper $y = H/2$ wall. To this end, consider Fig. 2(a) and the imposition of the condition at the indicated $(x_b, H/2)$ point. Applying Eq. (7) with $\beta = 1$, the contribution of reflected particles' integral in Eq. (10) becomes

$$\int_{\boldsymbol{\xi} \cdot \hat{\mathbf{n}} > 0} (\boldsymbol{\xi} \cdot \hat{\mathbf{n}}) f_{\text{uw}} \text{d}\boldsymbol{\xi} = \frac{\rho_{\text{uw}}(x_b)}{2\sqrt{\pi}}, \tag{11}$$

where the subscript "uw" denotes that the function is evaluated at a point along the upper wall. A less straightforward calculation is required to obtain the contribution of the incoming particles appearing in the $\boldsymbol{\xi} \cdot \hat{\mathbf{n}} < 0$ integral in Eq. (10). Here, particles may arrive from the inlet section, outlet section, lower $y = -H/2$ tunnel wall (lw), or upper plate surface (up), whereas no particles are transmitted directly from the "obscured" lower plate surface (lp). This is illustrated in Fig. 2(a), where the dashed blue lines confine channel domains of particles arriving from the different boundaries to $(x_b, H/2)$. Kinematically, these lines enclose the ξ_x/ξ_y ratios of in-plane molecular velocity components pertaining to particles' emittance from each surface.

Considering the contribution of particles reflected from the lower wall $(y = -H/2)$ along $-L/2 \leq x < x_l$ or $x_r < x \leq L/2$ [see Fig. 2(a)], we obtain

$$\int_{\boldsymbol{\xi} \cdot \hat{\mathbf{n}} < 0} (\boldsymbol{\xi} \cdot \hat{\mathbf{n}}) f_{\text{lw}} \text{d}\boldsymbol{\xi}$$

$$= -\frac{H^2}{4\sqrt{\pi}} \left(\int_{-L/2}^{x_l} \frac{\rho_{\text{lw}}(x) \text{d}x}{\left[H^2 + (x - x_b)^2\right]^{3/2}} + \int_{x_r}^{L/2} \frac{\rho_{\text{lw}}(x) \text{d}x}{\left[H^2 + (x - x_b)^2\right]^{3/2}} \right), \tag{12}$$
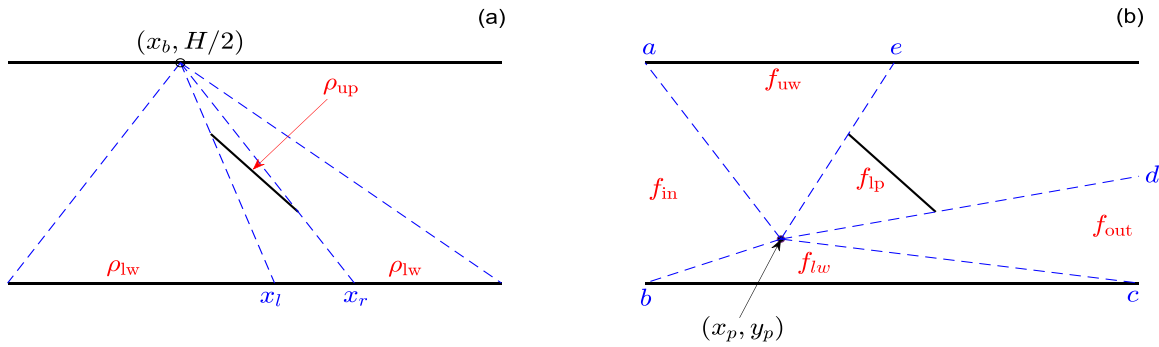
FIG. 2. Division of a diffuse-wall channel for the (a) imposition of the impermeability condition at a point $(x_b, H/2)$ along the upper $y = H/2$ tunnel wall, and (b) calculation of the hydrodynamic fields at a point (x_p, y_p) in the channel. The points $(x_b, H/2)$ and (x_p, y_p) in (a) and (b), respectively, are marked by circles and the dashed blue lines divide the channel into separate domains of particles arriving from the different boundaries.

whereas particles emitted from the upper plate surface contribute

$$
\int_{\boldsymbol{\xi}\cdot\hat{\mathbf{n}}<0}(\boldsymbol{\xi}\cdot\hat{\mathbf{n}})f_{\mathrm{up}}\mathrm{d}\boldsymbol{\xi}
$$
$$
= -\frac{1}{4\sqrt{\pi}}\int_{-1/2}^{1/2}\rho_{\mathrm{up}}(z)\frac{(z\sin\alpha + H/2)(x_b\sin\alpha + (H\cos\alpha)/2)}{\left[(z\sin\alpha + H/2)^2 + (x_b - z\cos\alpha)^2\right]^{3/2}}\mathrm{d}z.
$$

$$(13)$$

In Eq. (12), $x_{l,r} = x_b - H(2x_b \pm \cos\alpha)/(H \mp \sin\alpha)$ are the respective left and right x-coordinates confining the lower-wall segments that affect the upper wall at $x = x_b$. In cases where $x_l < -L/2$ or $x_r > L/2$ [not shown in Fig. 2(a)], only the right or left segments of the lower boundary transmit particles to the point of interest at the upper wall, respectively. In Eq. (13), z is a variable of integration along the plate upper surface and the integrand expectedly vanishes for $x_b = 0$ and $\alpha = \pi/2$. At sufficiently large angles of attack and at points relatively close to the left edge of the upper wall, there may be a wall interval for which the upper part of the plate becomes obscured and particles arrive from the plate lower surface. In such cases, f_{up} and ρ_{up} in Eq. (13) are replaced by f_{lp} and ρ_{lp}, respectively.

The contributions of particles arriving at (x_b, H_t) directly from the inlet or outlet sections are given by

$$
\int_{\boldsymbol{\xi}\cdot\hat{\mathbf{n}}<0}(\boldsymbol{\xi}\cdot\hat{\mathbf{n}})f_{\mathrm{in}}\mathrm{d}\boldsymbol{\xi} = \frac{1}{4\sqrt{\pi}}\left(\frac{L/2+x_b}{\sqrt{H^2+(L/2+x_b)^2}}-1\right) \quad (14)
$$

and

$$
\int_{\boldsymbol{\xi}\cdot\hat{\mathbf{n}}<0}(\boldsymbol{\xi}\cdot\hat{\mathbf{n}})f_{\mathrm{out}}\mathrm{d}\boldsymbol{\xi} = \frac{\rho_{\mathrm{out}}\sqrt{T_{\mathrm{out}}}}{4\sqrt{\pi}}\left(\frac{L/2-x_b}{\sqrt{H^2+(L/2-x_b)^2}}-1\right), \quad (15)
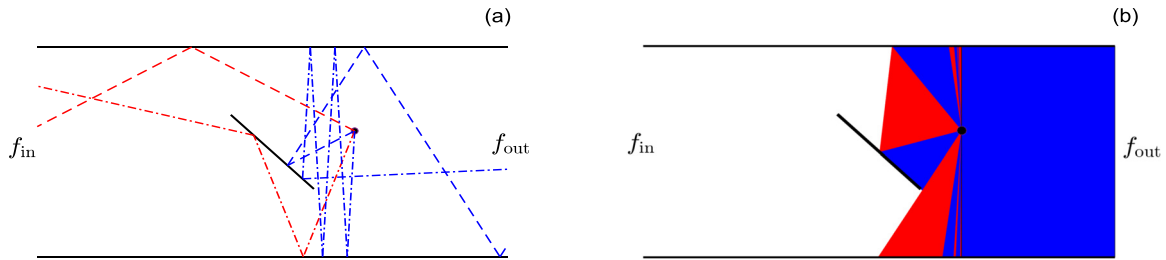$$

respectively. While these expressions correspond to the case illustrated in Fig. 2(a), where particles may arrive at $(x_b, H/2)$ from any point along the inlet and outlet sections, these sections may be partly obscured by the airfoil at other locations along the upper wall, which complicates the limits of integration and resulting expressions. Since these geometrical details may be easily retrieved, their tabulation is skipped here. Summing Eqs. (11)–(15) in Eq. (10), we obtain the impermeability condition at the point $(x_b, H/2)$ depicted in Fig. 2(a),

$$
2\rho_{\mathrm{uw}}(x_b) - H^2\left(\int_{-L/2}^{x_l}\frac{\rho_{\mathrm{lw}}(x)\mathrm{d}x}{\left[H^2+(x-x_b)^2\right]^{3/2}}+\int_{x_r}^{L/2}\frac{\rho_{\mathrm{lw}}(x)\mathrm{d}x}{\left[H^2+(x-x_b)^2\right]^{3/2}}\right)
$$
$$
- \int_{-1/2}^{1/2}\rho_{\mathrm{up}}(z)\frac{(z\sin\alpha + H/2)(x_b\sin\alpha + (H\cos\alpha)/2)}{\left[(z\sin\alpha + H/2)^2 + (x_b - z\cos\alpha)^2\right]^{3/2}}\mathrm{d}z
$$
$$
= -\left(\frac{L/2+x_b}{\sqrt{H^2+(L/2+x_b)^2}}-1\right)
$$
$$
- \rho_{\mathrm{out}}\sqrt{T_{\mathrm{out}}}\left(\frac{L/2-x_b}{\sqrt{H^2+(L/2-x_b)^2}}-1\right). \quad (16)
$$

Following similar arguments, the impermeability conditions over all other solid surfaces are derived, as detailed in Appendix A. These, together with Eq. (16), yield a set of coupled integral equations for the boundaries' density fluxes, where the inlet and outlet section contributions serve as non-homogeneous forcing terms. In the case where the inlet and outlet reservoirs are kept at the same state, i.e., $\rho_{\mathrm{in}} = T_{\mathrm{in}} = \rho_{\mathrm{out}} = T_{\mathrm{out}} = 1$, the expected uniform $\rho_{\mathrm{uw}} = \rho_{\mathrm{lw}} = \rho_{\mathrm{up}} = \rho_{\mathrm{lp}} = 1$ solution is obtained. For any non-trivial combination of $0 \leq \rho_{\mathrm{out}} \leq 1$ and $0 < T_{\mathrm{out}} \leq 1$, the impermeability conditions were solved numerically by discretizing the fluxes along the boundaries. To this end, the fluxes were represented by their discrete values at equally spaced points along the walls, with the integral terms evaluated using the trapezoidal rule. This resulted in a system of linear coupled non-homogeneous algebraic equations that was inverted using a MATLAB subroutine. Converged results were derived with a scaled discretization step of $\approx 10^{-3}$ along the solid surfaces, constituting a minor computational effort compared with the numerical DSMC calculations described in Sec. IV.

Having calculated the fluxes, the probability density function in Eq. (9) is known, and the hydrodynamic fields may be calculated via appropriate quadratures over the velocity space. Specifically, the density ρ and x- and y-velocity components u_x and u_y are given by[28]

$$
\rho(x,y) = \int_{-\infty}^{\infty}f\mathrm{d}\boldsymbol{\xi}, \quad u_x(x,y) = \frac{1}{\rho(x,y)}\int_{-\infty}^{\infty}\xi_x f\mathrm{d}\boldsymbol{\xi}, \text{ and } u_y(x,y)
$$
$$
= \frac{1}{\rho(x,y)}\int_{-\infty}^{\infty}\xi_y f\mathrm{d}\boldsymbol{\xi}, \quad (17)
$$

FIG. 3. (a) Specular-wall particle trajectories originating at the inlet (dashed and dashed-dotted red lines) and outlet (dashed and dashed-dotted blue lines) sections and arriving at $(x, y) = (0.7, 0.2)$. (b) Division of a specularly reflecting channel into sections of particles originating at the tunnel inlet (red) and outlet (blue) sections and arriving at $(x, y) = (0.7, 0.2)$ (denoted by the black circle). In both (a) and (b), a channel of length $L = 4$ and height $H = 2$ is considered with a plate set at $\alpha = \pi/4$.

respectively, and the normal (P_{xx}, P_{yy}, and P_{zz}) and shear (P_{xy}) stresses are computed via

$$P_{xx}(x,y) = \int_{-\infty}^{\infty} (\xi_x - u_x)^2 f \mathrm{d}\xi, \quad P_{yy}(x,y) = \int_{-\infty}^{\infty} (\xi_y - u_y)^2 f \mathrm{d}\xi,$$

$$P_{zz}(x,y) = \int_{-\infty}^{\infty} \xi_z^2 f \mathrm{d}\xi, \quad \text{and} \quad P_{xy}(x,y) = \int_{-\infty}^{\infty} (\xi_x - u_x)(\xi_y - u_y) f \mathrm{d}\xi,$$

(18)

respectively. The pressure field is obtained by superposing the normal stresses,

$$p(x,y) = \frac{2}{3}(P_{xx} + P_{yy} + P_{zz}),$$

whereas the temperature $T = p/\rho$, in accordance with the scaled ideal-gas equation of state. At each (x, y) location, the above integrations average the contributions of particles arriving from the various boundaries, in accordance with the setup geometry. Similar to the calculation of boundary fluxes, particles may arrive at a given location from only part of the channel boundaries, while others are obscured. This is illustrated in Fig. 2(b), where the tunnel is divided into five sections of particles arriving at the indicated (x_p, y_p) point from the inlet, outlet, lower wall, upper wall, or lower plate sections. While particles arrive at (x_p, y_p) from all points along the inlet and lower wall boundaries, the upper wall and outlet sections are partly obscured and no particles may be emitted directly from the upper plate surface. The integrations specified in Eqs. (17) and (18) are carried out in accordance with the geometrical restrictions at each location, to yield the required (x, y) distributions of the hydrodynamic fields across the tunnel.

Omitting intermolecular gas interactions, the information on a surface presence is transferred to the gas directly by particles that have collided with the solid boundary at an earlier time. Thus, the population of particles arriving from a given solid wall at each channel location is kinematically delineated as shown in Fig. 2(b). This determines the respective molecular-velocity-space interval that is averaged in the calculation of hydrodynamic fields and affects the macroscopic gas behavior. With increasing distance from a surface, this interval narrows, reflecting the diminishing geometrical impact of the boundary.

B. Specular reflecting walls

Different from the diffuse-scattering [$\beta = 1$ in Eq. (7)] case, the macroscopic impermeability conditions are trivially satisfied at a specular reflecting surface ($\beta = 0$), where the particles undergo mirror-like reflections with the value of the velocity distribution function preserved. The particles in the tunnel consequently acquire either the inlet or outlet Maxwellian distributions [see Eq. (8)], and the problem solution reduces to sorting, at each (x, y) location, between these distributions, based on the direction of the in-plane (ξ_x, ξ_y) velocity vector of the particle. To track the origin of a particle located at a given point, its trajectory should be traced backward to either the inlet or outlet sections where it has entered the tunnel. This is illustrated in Fig. 3(a), where several particle trajectories originating at the inlet (red lines) and outlet (blue curves) sections, and arriving at $(x, y) = (0.7, 0.2)$, are plotted in a tunnel of length $L = 4$ and $H = 2$ (to be studied later on). When followed in all directions at the chosen location, the sorting procedure yields the colormap presented in Fig. 3(b), showing the division of this channel into sections of particles originating at the inlet (in red) or outlet (in blue) sections and arriving at $(x, y) = (0.7, 0.2)$. The calculation should be repeated at all (x, y) locations of interest, to determine the solution for $f(x, y, \xi)$ in the five-dimensional phase space. The hydrodynamic fields are then calculated by the quadratures specified in Eqs. (17) and (18).

IV. NUMERICAL SCHEME: DSMC METHOD

The DSMC method is the most widely used scheme for simulating non-equilibrium gas flows. The method was initially introduced for gas simulations as a direct numerical approach for calculating the dynamics of a dilute gas,[30] which was later on shown to yield results that converge to the solution of the Boltzmann equation.[31] Within the DSMC framework, the velocity distribution function of the gas molecules is represented by a number of computational particles. The computational domain is divided into a mesh of cells whose size Δs^* is smaller than the particles' mean free path λ^*. The particles' motions and interactions are decoupled over a time step Δt^*, being shorter than the local mean free time τ^* between collisions. At each time step, the particles are first translated following "free-flight" kinematics, as if they do not interact with each other. Then, the particles are sorted into computational cells and collisions are evaluated stochastically, conserving the collision momentum and energy invariants. The computational cells are used for evaluating the macroscopic fields, which are obtained through weighted averages of the particles properties.

In the present work, we apply the DSMC algorithm to analyze the airfoil tunnel problem for arbitrary, and particularly large, Knudsen numbers (Kn = $\lambda^*/c^* \gg 1$). The interaction between the gas molecules was calculated based on the commonly used

hard-sphere model of molecular interaction. The effect of other models of interaction, expected to affect the results quantitatively,[32] was not considered herein. The two-dimensional computational domain was divided into cells of equal size not exceeding $\Delta x^* = 0.05\lambda^*$, and the time step was set no larger than $\Delta t^* = 0.01\tau^*$. At the initial state, the simulation domain contained no particles. Then, at each time step, computational particles were inserted from the outlet and inlet sections, by sampling the flux of the Maxwellian distributions specified in Eq. (1). Computational particles crossing the inlet and outlet boundaries from inside the tunnel were removed from the simulation domain, and diffuse or specular reflections were applied to describe the scattering from the channel and plate solid walls. The simulation was followed until a steady state was formed, by letting the transient behavior evolve into a time-independent solution. The calculation of macroscopic quantities commenced after a steady state was reached, with the sampling time duration determined by requiring that the relative statistical error does not exceed 0.05 of the signal. A typical calculation was carried out with a computational grid of ≈ 200 cells in the x-direction and ≈ 100 cells in the y-direction for a channel of size $L = 4$ and $H = 2$ in plate-length units. Taking ≈ 200 particles per cell, a sample of $\approx 4 \times 10^6$ particles was considered. Each computation lasted a few hours using a single processor Intel® Core™ i7-11800 machine (24 M Cache, up to 4.60 GHz). To verify the accuracy of results, a convergence analysis (not detailed here for brevity) was carried out. This has indicated that our simulation predictions are nearly unaffected by further decrease in the above-mentioned cells' size and time step or by an increase in the number of particles taken per cell, thus ensuring the grid independence of our DSMC predictions.

V. RESULTS AND DISCUSSION

To present our findings, we consider primarily a tunnel of length and width

$$L = 4 \quad \text{and} \quad H = 2, \qquad (19)$$

respectively, in plate chord units. Channel dimensions of order unity are taken to comply with our focus on high-Kn number flows, where the Knudsen number is based on the unity-scaled airfoil size [see Eq. (5)]. Having fixed L and H, the problem is governed by the airfoil angle of attack α and outlet reservoir conditions ρ_{out} and T_{out}, as well as by the value of the Knudsen number and the type of wall conditions (diffuse or specular). These effects are studied below, where the validity and breakdown of the free-molecular description are tested via comparison of the collisionless solution with DSMC predictions at finite Knudsen numbers. In Sec. V A, the density-driven problem ($0 \leq \rho_{out} < 1, T_{out} = 1$) is investigated, followed by the temperature-driven setup ($\rho_{out} = 1, 0 < T_{out} < 1$) in Sec. V B. The impact of channel wall separation (increasing H) is considered in Sec. V C, to examine the convergence of the solution to the free-stream limit and quantify the impact of sidewall tunnel reflections on the predicted gas loading on the plate.

A. Density-driven flow

Figure 4 presents two-dimensional colormaps of the free-molecular density [Fig. 4(a)], velocity amplitude [Fig. 4(b)], temperature, [Fig. 4(c)] and pressure [Fig. 4(d)] fields for an airfoil set at an angle of attack $\alpha = \pi/4$ in a diffuse-wall tunnel with $\rho_{out} = 0.2$ and $T_{out} = 1$. The thick solid lines indicate the plate and tunnel wall locations and the blue curves in Fig. 4(b) show the flow streamlines. Although a high angle of attack is considered, the free-molecular flow field is found fully attached to the plate, satisfying the impermeability condition over the solid surface. At the imposed density gradient, a maximum gas speed of ≈ 0.27 in most-probable-speed units is viewed close to the airfoil tips and across the channel outlet section. This is equivalent to a slightly higher subsonic Mach number of
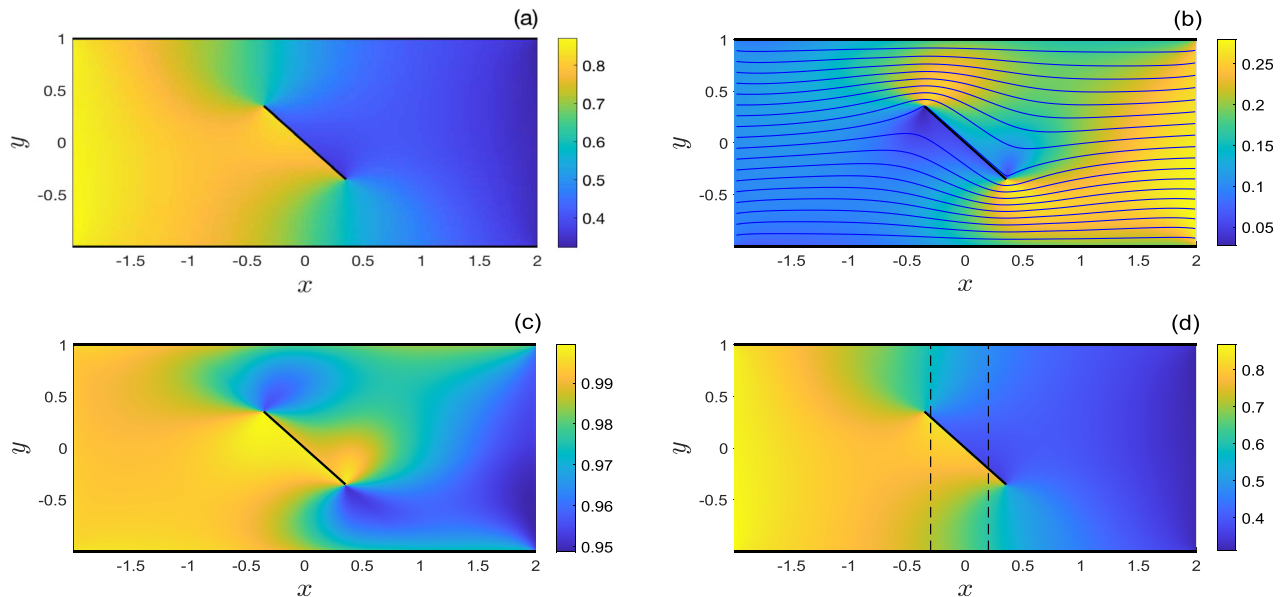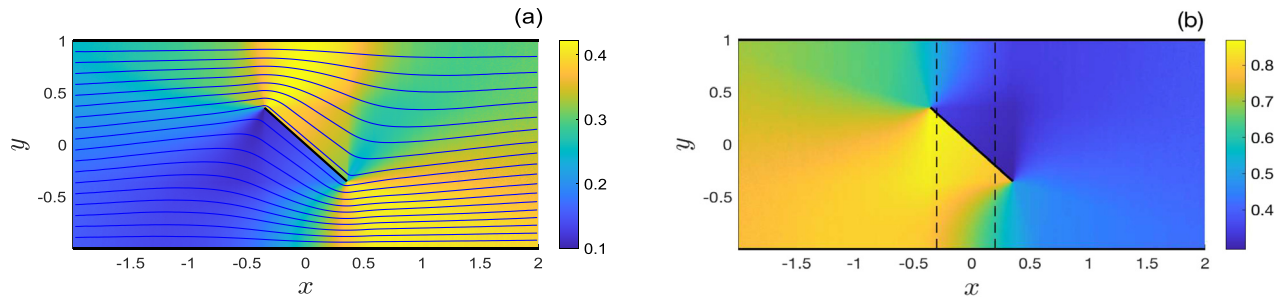
FIG. 4. Colormaps of the free-molecular (a) density, (b) velocity magnitude, (c) temperature, and (d) pressure fields for an airfoil set at $\alpha = \pi/4$ in a diffuse-wall tunnel with $\rho_{out} = 0.2$ and $T_{out} = 1$. The thick lines mark the plate location and tunnel walls, and the blue curves in (b) show the flow streamlines. The dashed vertical lines in (d) mark the $x = -0.3$ and $x = 0.2$ sections along which the results in Fig. 6 are presented.

FIG. 5. Colormaps of the free-molecular (a) velocity magnitude and (b) pressure fields for an airfoil set at $\alpha = \pi/4$ in a specular-wall tunnel with $\rho_{\text{out}} = 0.2$ and $T_{\text{out}} = 1$. The thick lines mark the plate location and tunnel walls, and the blue curves in (a) indicate the flow streamlines. The dashed vertical lines in (b) mark the $x = -0.3$ and $x = 0.2$ sections along which the results in Fig. 6 are presented.

$\approx 0.27\sqrt{2/\gamma} \approx 0.3$ (with a heat capacity ratio of $\gamma = 5/3$ for an ideal monatomic gas). Examining Fig. 4(c), the density-driven flow field is seen nearly isothermal, yielding density and pressure fields that are largely identical. A pressure jump of typically $\Delta p = p_{\text{lower}} - p_{\text{upper}} \approx 0.35$ (in $\rho_{\text{in}}^* U_{\text{mp}_{\text{in}}}^{*2}$ units) is observed across the plate in Fig. 4(d) [cf. Fig. 6(c)], reflecting the high and low densities characterizing the upstream and downstream parts of the channel, respectively. Notably, and as allowed by the free-molecular conditions, while the flow is roughly stagnant along the lower plate surface, significant slip (of speed $\gtrsim 0.1$) is observed along the upper airfoil boundary.

Figure 5 studies the effect of tunnel and plate surface conditions on the system behavior. Maintaining the same geometrical and outer reservoir state as in Fig. 4, and replacing the diffuse- with specular-wall conditions over all solid boundaries, the figure presents colormaps of the corresponding free-molecular velocity magnitude [Fig. 5(a)] and pressure [Fig. 5(b)] fields. Comparing with Fig. 4(b), considerably higher speeds (reaching ≈ 0.42, equivalent to a Mach number of ≈ 0.46) are observed, accompanied by larger velocity slip along the airfoil and tunnel wall surfaces. These reflect the specular-wall interactions, where no kinetic energy is absorbed by the solid stationary walls, in contrast to the diffuse-wall setup. Higher pressure jumps are observed in the specular-wall case, reaching $\Delta p \approx 0.5$ [cf. Figs. 6(c) and 6(d)]. These, in turn, are replicated in the differences between the integral aerodynamic forces acting on the plate in the diffuse- and specular-wall configurations, as studied below. Generally, more pronounced flow gradients characterize the flow close to the airfoil tips in the specular-wall setup. These are associated with the more confined zone that is kinematically affected by emittance of gas particles from the airfoil surface, which is different from the smoother particle dispersion in the diffuse-wall configuration.

The validity of our free-molecular description is examined in Fig. 6, where the collisionless results are compared with DSMC predictions at finite Knudsen numbers. Considering $x = -0.3$ and $x = 0.2$ as representative sections [marked by the dashed lines in Figs. 4(d) and 5(b)], the figure shows y-distributions of the x-velocity [Figs. 6(a) and 6(b)] and pressure [Figs. 6(c) and 6(d)] fields for both diffuse- [Figs. 6(a) and 6(b)] and specular-wall [Figs. 6(c) and 6(d)] setups. In each case, the ballistic results are compared with DSMC calculations at Kn = 10, 2, and 1. The dashed lines in each figure connect adjacent data points from opposite sides of the airfoil, where discontinuous "jumps" in the hydrodynamic fields occur.

Considering the diffuse-wall results in Figs. 6(a) and 6(c), it is noted that the agreement between ballistic and DSMC predictions is excellent at Kn = 10 (marked by the triangles) and slightly diminishes with decreasing Kn. Still, the free-molecular results match very well even with Kn = 1 DSMC data, indicating that the effect of molecular collisions remains minor up to Kn $\gtrsim 1$ in the diffuse-wall and relatively narrow ($H = 2$) channel setup considered. Traversing to the specular-wall comparison, we observe that the breakdown of the free-molecular description is markedly more visible at Kn $\sim O(1)$, yet the DSMC results unequivocally converge to the collisionless limit with increasing Kn. Recalling that the present Knudsen definition is based on the airfoil size [see Eq. (5)], it is effectively smaller if based on the channel width ($H = 2$) or length ($L = 4$). In this respect, we consider the good agreement of both diffuse- and specular-wall ballistic results with DSMC predictions at Kn = 10 gratifying.

The results in Fig. 6 along $x = 0.2$ and $x = -0.3$ and the agreement obtained with DSMC predictions are inevitably affected by the tunnel and plate walls, since the y-coordinate initiates and terminates at the channel walls, $y = -1$ and $y = 1$. To put these findings in context, we have examined the validity and breakdown of the free-molecular solution in a reference empty channel configuration with decreasing Knudsen numbers. Representative results are shown in Fig. 7, where the free-molecular x-velocity component in a diffuse-wall tunnel is compared with DSMC data at the same Kn = 10, 2, and 1 along $x = 0.2$ and $x = -0.3$, as in Fig. 6. Similar to Fig. 6, the results indicate that the free-molecular description remains valid at large yet finite Knudsen numbers and provides a fair approximation through Kn $\gtrsim 1$, where discrepancies reach up to $\approx 4.5\%$. The Knudsen number referred to in the figure, in the absence of the plate, is based on half the channel width.

A key output of any wind tunnel measurement are the aerodynamic forces acting on the tested body, obtained via integration of the normal and shear stresses along the body surface. In the present setup, the $\rho_{\text{in}}^* U_{\text{mp}_{\text{in}}}^{*2} c^*$-scaled y-directed lift force on the plate per unit span is given by

$$L = \int_{-0.5}^{0.5} \left[\left(P_{s_\perp s_\perp}(s_\parallel, s_\perp = 0^-) \cos \alpha - P_{s_\parallel s_\perp}(s_\parallel, s_\perp = 0^-) \sin \alpha \right) \right.$$
$$\left. - \left(P_{s_\perp s_\perp}(s_\parallel, s_\perp = 0^+) \cos \alpha - P_{s_\parallel s_\perp}(s_\parallel, s_\perp = 0^+) \sin \alpha \right) \right] ds_\parallel, \tag{20}$$

where $s_\parallel$ and $s_\perp$ denote the body coordinates (with origin at the plate midchord) parallel and normal to the surface, respectively. The stress
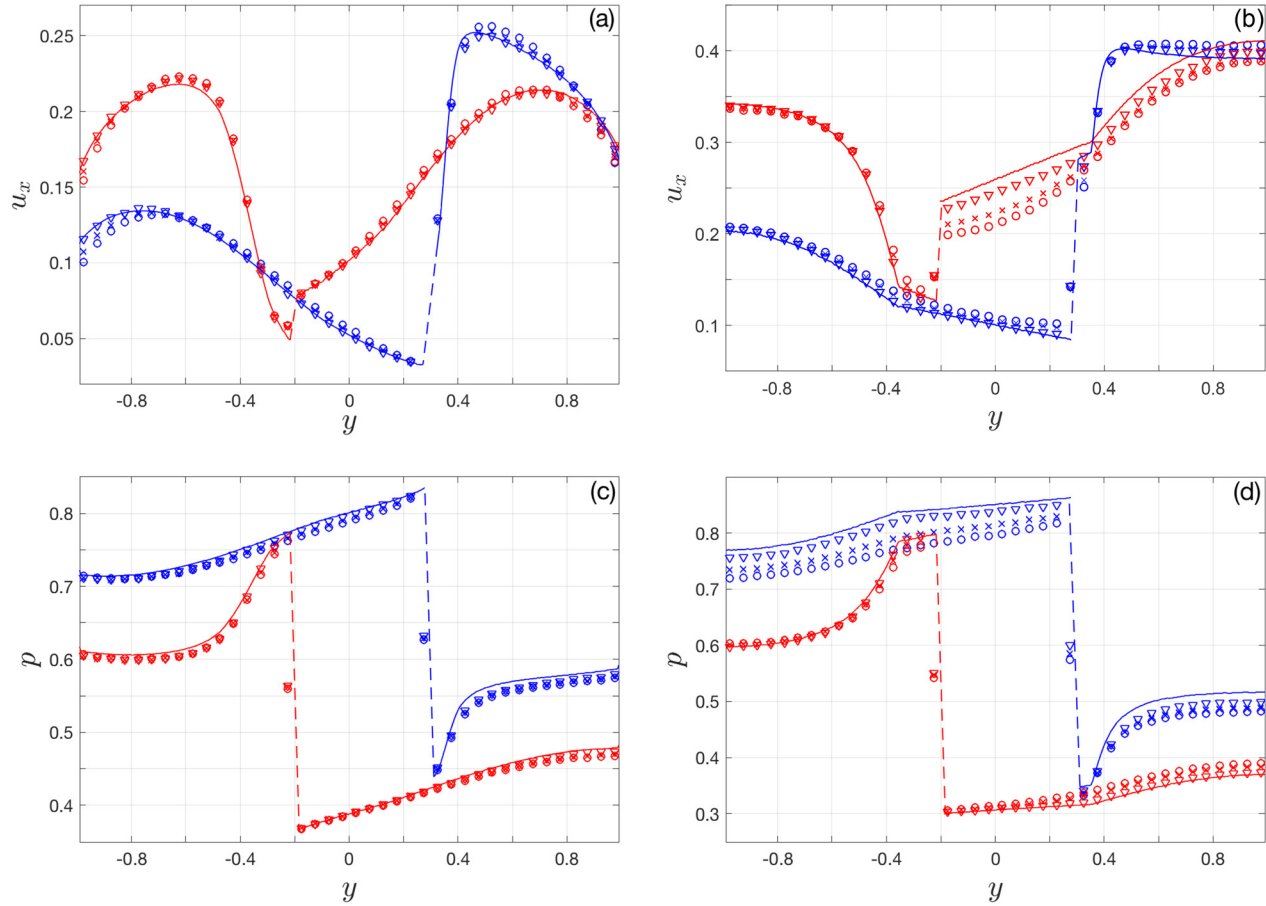
FIG. 6. Comparison between free-molecular (solid lines) and DSMC predictions (symbols) for the x-velocity (a) and (b) and pressure (c) and (d) fields along $x = -0.3$ (in blue) and $x = 0.2$ (in red). (a) and (c) show results for a diffuse-wall channel and (b) and (d) present data for a specular tunnel. The triangles, crosses, and circles show DSMC data at Kn = 10, 2, and 1, respectively. All results are for an airfoil set at $\alpha = \pi/4$ in a tunnel with $\rho_{\text{out}} = 0.2$ and $T_{\text{out}} = 1$. The dashed lines connect free-molecular data points at opposite sides of the airfoil.

components appearing in Eq. (20) are the normal ($P_{s_\perp s_\perp}$) and shear ($P_{s_\parallel s_\perp}$) stress fields at the plate, calculated via Eq. (18) after replacing all x and y indices by $s_\parallel$ and $s_\perp$, respectively. The counterpart x-directed scaled drag force on the airfoil is calculated via

$$
D = \int_{-0.5}^{0.5} \left[\left(P_{s_\perp s_\perp}(s_\parallel, s_\perp = 0^-) \sin\alpha + P_{s_\parallel s_\perp}(s_\parallel, s_\perp = 0^-) \cos\alpha \right) \right.
$$
$$
\left. - \left(P_{s_\perp s_\perp}(s_\parallel, s_\perp = 0^+) \sin\alpha + P_{s_\parallel s_\perp}(s_\parallel, s_\perp = 0^+) \cos\alpha \right) \right] ds_\parallel.
$$
$$(21)$$

The effect of problem parameters on the calculated forces is examined below.

Figure 8 presents the variations in free-molecular lift [Fig. 8(a)], drag [Fig. 8(b)], and lift-over-drag ratio [Fig. 8(c)] with the (scaled-by-π) plate angle of attack. Only the $0 \leq \alpha \leq \pi/2$ interval is presented since the $\pi/2 \leq \alpha \leq \pi$ part follows by symmetry. The results are shown for both diffuse- (solid lines) and specular-wall (dashed curves) tunnel configurations at the indicated values of ρ_{out} (with $T_{\text{out}} = 1$).

In Figs. 8(a) and 8(b), a comparison is made with DSMC predictions, indicating a close agreement between the free-molecular and numerical results at Kn = 10. In line with the comparison in Fig. 6, the deviation between collisionless and DSMC data with decreasing Kn is more visible in the specular-wall configuration, showing discernible differences at Kn = 2.

Examining Fig. 8(a), we observe that the lift varies non-monotonically with α in all cases, reaching a maximum at an intermediate value of plate inclination. Indeed, at $\alpha = 0$ and $\alpha = \pi/2$ the y-directed force vanishes due to problem symmetry. In between, plate inclination results in a finite positive lift force (becoming anti-symmetrically negative for $\pi/2 \leq \alpha \leq \pi$). In the diffuse-wall setup, all lift curves are nearly symmetric about $\alpha = \pi/4$, where their maxima are reached. In the specular-wall configuration, the maxima shift to somewhat lower α. With increasing density differences between the reservoirs, the lift force is magnified toward a limit value reached at expansion-to-vacuum ($\rho_{\text{out}} = 0$) conditions. This is marked by the thin magenta curve that is nearly identical with the $\rho_{\text{out}} = 0.01$ result. As expected, the lift force in the specular-channel setup is invariably
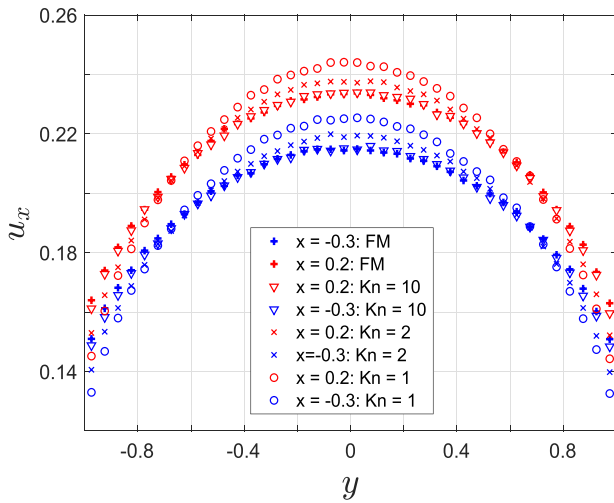
FIG. 7. Comparison between free-molecular (pluses) and DSMC predictions (other symbols) for the x-velocity field along $x = -0.3$ (in blue) and $x = 0.2$ (in red) in a diffuse-wall channel in the absence of a plate. The triangles, crosses, and circles show DSMC data at Kn = 10, 2, and 1, respectively. All results are for a channel with $\rho_{out} = 0.2$ and $T_{out} = 1$ and the Knudsen number is based on half the channel width. The channel dimensions, $H = 2$ and $L = 4$, are kept as in previous figures discussions.

larger than in the counterpart diffuse-wall case. In terms of flow velocities, our results indicate that maximum speeds are observed in the limit $\rho_{out} = 0$ case, where $|\mathbf{u}| \approx 0.6$ and $|\mathbf{u}| \approx 0.79$ are found in the vicinity of plate edges in the diffuse- and specular-wall configurations, respectively. These correspond to respective mean speeds of $|\mathbf{u}| \approx 0.25$ and $|\mathbf{u}| \approx 0.39$ at the tunnel inlet section. Limited by the vacuum conditions at the outlet, the above subsonic velocity magnitudes should be considered as the maximum speeds that may be reached in the present tunnel configuration. Higher flow velocities may be examined by considering different types of inlet and outlet conditions (see Sec. V C), or by modifying the tunnel geometry (see Sec. VI), which is beyond the scope of the present study.

Different from the lift, the drag force in Fig. 8(b) increases monotonically with α for $0 \leq \alpha \leq \pi/2$, reaching a maximum at $\alpha = \pi/2$ that symmetrically drops for $\pi/2 \leq \alpha \leq \pi$. In the specular-wall setup, the drag is vanishing at $\alpha = 0$, since $P_{xy}(s_\perp = 0^\pm; \alpha = 0) \equiv 0$ over the smooth surface. A finite drag force is observed at $\alpha = 0$ in the diffuse-wall case, reflecting the integral transfer of energy between the gas and the plate at $\beta = 1$. Inspecting Eq. (21), it is clear that the drag force becomes dominated by the normal $P_{s_\perp s_\perp}$ contribution with increasing α, whereas the $P_{s_\parallel s_\perp}$ terms (multiplied by $\cos \alpha$) vanish at $\alpha = \pi/2$. This is different from the lift variation in Eq. (20), where both $P_{s_\perp s_\perp}$ and $P_{s_\parallel s_\perp}$ contributions vanish as $\alpha \to \pi/2$, either due to their α dependence or because of flow symmetry. In line with the observations for lift loading, the drag force in the diffuse-wall case is smaller than in the specular wall system, apart from small α values where the vanishing of $P_{xy}(s_\perp = 0^\pm; \alpha \ll 1)$ in the specular configuration reduces its value below its diffuse-wall counterpart [cf. the dashed and solid lines in Fig. 8(b) for $\alpha/\pi \lesssim 0.1$].

The lift-to-drag ratio in Fig. 8(c) shows qualitative different trends between the specular- (dashed line) and diffuse-wall (solid curve) systems. Thus, the L/D ratio decreases monotonically with α in the specular case at a given ρ_{out}, starting from an unbounded value at $\alpha \to 0$ and vanishing as $\alpha \to \pi/2$. In the diffuse-wall setup, L/D vanishes at both $\alpha = 0$ and $\alpha = \pi/2$ end points and reaches a maximum of $L/D \approx 1$ value at $\alpha \approx 0.11\pi$. In each configuration, all L/D curves collapse over a single line, regardless of the value of ρ_{out}. This reflects the linear dependence of all Maxwellians on the density, which cancels out by division of the lift by the drag. The main qualitative difference between the specular and diffuse setups, being the divergence and vanishing of L/D for $\alpha \ll 1$ between the two cases, respectively, follows from the vanishing of $P_{xy}(s_\perp = 0^\pm; \alpha = 0)$ in the specular case, resulting in a singular value for the specular lift-to-drag ratio as $\alpha \to 0$.

B. Temperature-driven flow

To study the plate aerodynamics in a temperature-driven flow setup, Fig. 9 presents the free-molecular velocity [Fig. 9(a)] and pressure [Fig. 9(b)] fields in a diffuse-wall tunnel with $T_{out} = 0.2$ and $\rho_{out} = 1$ for the same $\alpha = \pi/4$ and tunnel dimensions studied in Fig. 4. While the pressure ratio between the reservoirs is identical between Figs. 4 and 9 ($p_{out}^*/p_{in}^* = 0.2$), we observe that considerably lower flow speeds and pressure variations are obtained within the tunnel in the temperature-driven case. To rationalize that, we first consider the effect of outlet reservoir conditions on tunnel permeability and then study their impact on the aerodynamic loadings on the plate.

At a given pressure ratio, temperature-driven channel flows at high Knudsen numbers are known to generate lower mass flow rates compared with their density-driven counterparts. In terms of the present scaling, the mass flow rate per unit length through the tunnel is given by

$$\dot{m} = \int_{-H/2}^{H/2} \rho(x,y) u_x(x,y) \mathrm{d}y, \qquad (22)$$

where the result should be independent of x, in line with flow mass conservation. For the simple case of a straight channel with specular walls (in the absence of an airfoil), it is known that[33]

$$\dot{m}^{(\text{no-airfoil,spec})} = \frac{H}{2\sqrt{\pi}} \left(1 - \rho_{out} \sqrt{T_{out}} \right), \qquad (23)$$

predicting higher flow rates in density- compared with temperature-driven flows at a fixed $p_{out} = \rho_{out} T_{out}$.

Considering the current configuration, Fig. 9(c) presents the variation of $\dot{m}$, calculated using Eq. (22), with the airfoil angle of attack in diffuse- (solid lines) and specular-wall (dashed lines) tunnels. Results for the above-studied density-driven ($\rho_{out} = 0.2$, blue lines) and temperature-driven ($T_{out} = 0.2$, red curves) configurations are compared. At $\alpha = 0$, the mass flow rate in a specular channel coincides with the value predicted by Eq. (23) and marked by triangles. Thus, $\dot{m} \approx 0.451$ for $\rho_{out} = 0.2$ and $\dot{m} \approx 0.312$ for $T_{out} = 0.2$. The mass flow rate then decreases monotonically for $0 \leq \alpha \leq \pi/2$, reflecting the partial blockage caused by the airfoil. In agreement with the above discussion and in both specular- and diffuse-wall configurations, $\dot{m}$ is uniformly larger in the density-driven compared with the temperature-driven setup. Additionally, the mass flow rate in a diffuse-wall setup is lower than in the counterpart specular tunnel, indicating a reduction in flow momentum due to exchange of gas kinetic energy with the diffuse surfaces. The free-molecular results are well supported

02 May 2024 14:08:11
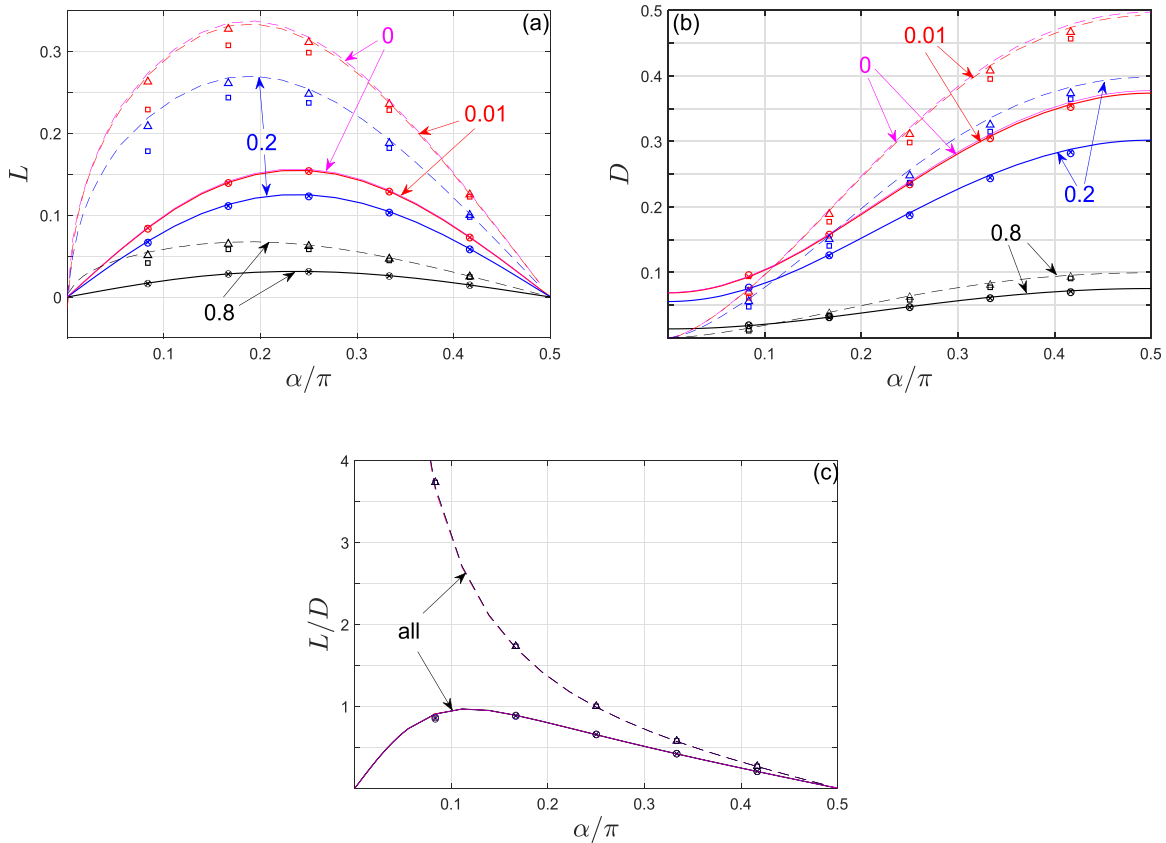
FIG. 8. Variations of the free-molecular (a) lift, (b) drag, and (c) lift-to-frag force ratio with the plate scaled angle of attack α/π for diffuse- (solid lines) and specular-wall (dashed curves) tunnels at the indicated values of ρ_{out} (with $T_{\text{out}} = 1$). The crosses and circles mark DSMC results in a diffuse-wall tunnel with Kn = 10 and 2, respectively, whereas the triangles and squares denote the counterpart data in a specular-wall configuration.

by the presented DSMC data at Kn = 10. Overall, and for the present $H = 2$ choice of tunnel width, the high-Knudsen mass flow rate reduces by $\approx 50\%$ between $\alpha = 0$ and $\alpha = \pi/2$ in the specular-wall configurations and by slightly more than $\approx 35\%$ for the diffuse-wall setups.

Reverting to the aerodynamic problem, Fig. 10 presents the effect of outlet reservoir conditions on the variations of the free-molecular lift [Fig. 10(a)] and lift-over-drag ratio [Fig. 10(b)] with the plate incidence in a diffuse-wall tunnel. Results for both density-driven (solid lines) and temperature-driven (dashed curves) configurations are shown. A comparison is made with counterpart DSMC predictions at Kn = 10, showing close agreement. Considering Fig. 10(a) and in line with the discussion of Fig. 9, we observe that the lift force at a given outlet pressure (being $p_{\text{out}} = 0.8$ or $p_{\text{out}} = 0.2$) is smaller in the temperature-driven compared with the density-driven case. Inspecting Fig. 10(b), and different from the single-curve collapse of all curves in the density-driven case [cf. the solid red line herein and the results in Fig. 8(c)], we find that the lift-over-drag ratio varies between different values of T_{out}, approaching the density-driven curve with decreasing outlet temperature.[34] This reflects the nonlinear dependence of all Maxwellians on the temperature, which, unlike in the density-driven case, does not cancel out when dividing the lift by the drag.

Nevertheless, the non-monotonic variation of L/D is qualitatively similar in all cases, where maximum aerodynamic efficiency is achieved at an angle of attack slightly above $\alpha \approx 0.1\pi$.

C. The free-stream limit

In practice, the main advantage of using a wind tunnel facility is in its ability to predict the aerodynamic loadings over a given configuration at free-stream conditions without the necessity of carrying costly challenging real-flight tests. It is therefore of interest to study the correlation between our present calculations and the free-stream results in the ballistic flow regime.

We start by recapitulating the expressions for the collisionless free-stream aerodynamic loadings on a two-dimensional flat plate inclined at an angle α to a uniform flow of dimensionless speed U_0. For a diffuse-reflecting plate, the collisionless free-stream forces normal (F_N) and parallel (F_S) to the plate are expressed by[17,18]

$$F_N^{(\text{FS,diff})} = \frac{1}{2}\left[\left(2U_N^2 + 1\right)\text{erf}(U_N) + \frac{2}{\sqrt{\pi}}U_N\exp\left[-U_N^2\right] + \sqrt{\pi}U_N\right] \tag{24}$$

and
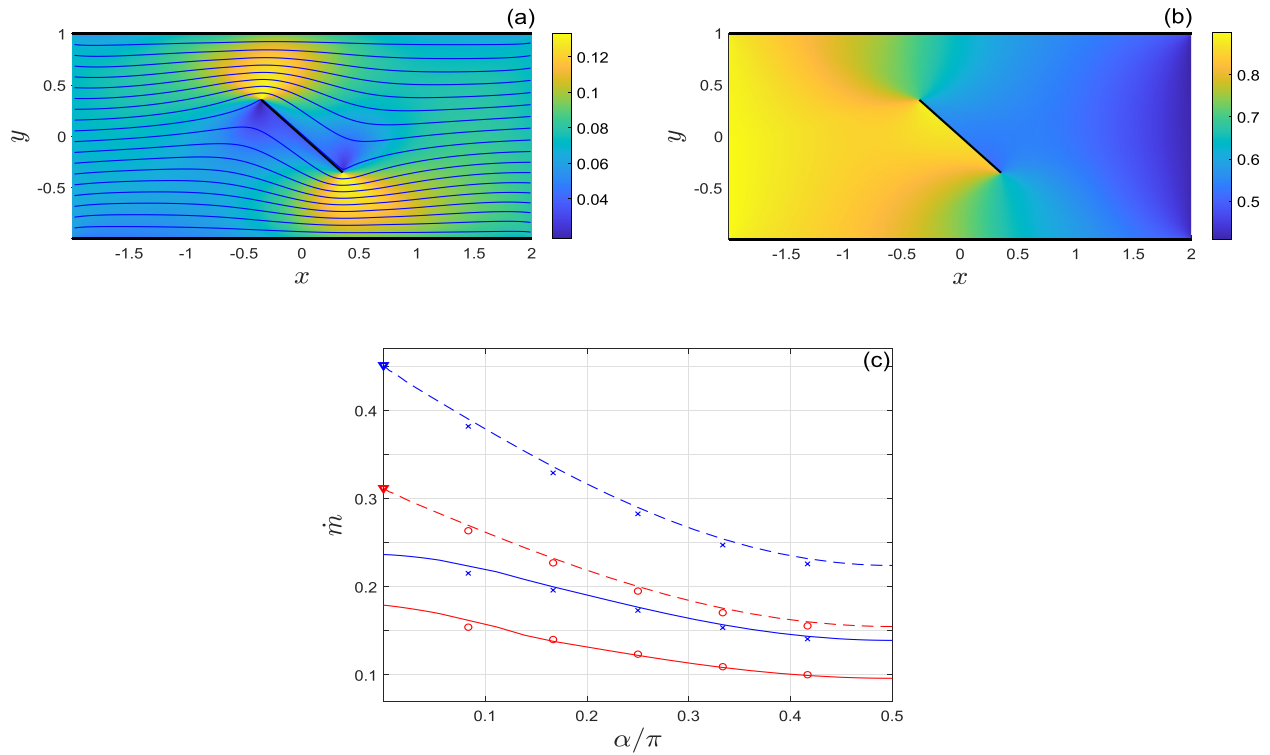
FIG. 9. Colormaps of the free-molecular (a) velocity magnitude and (b) pressure field over an airfoil set at $\alpha = \pi/4$ in a temperature-driven diffuse tunnel with $T_{out} = 0.2$ and $\rho_{out} = 1$. The thick lines mark the plate location and tunnel walls, and the blue curves in (a) show the flow streamlines. (c) Variations of the free-molecular tunnel mass flow rate with the airfoil angle of attack in diffuse- (solid lines) and specular-wall (dashed lines) channels. The blue and red curves show results for density-driven ($\rho_{out} = 0.2$, $T_{out} = 1$) and temperature-driven ($\rho_{out} = 1$, $T_{out} = 0.2$) setups, respectively, and the triangles at $\alpha = 0$ mark the free-molecular mass flow rates in a specular channel with no airfoil [see Eq. (23)]. The crosses and circles present respective DSMC results at Kn = 10.
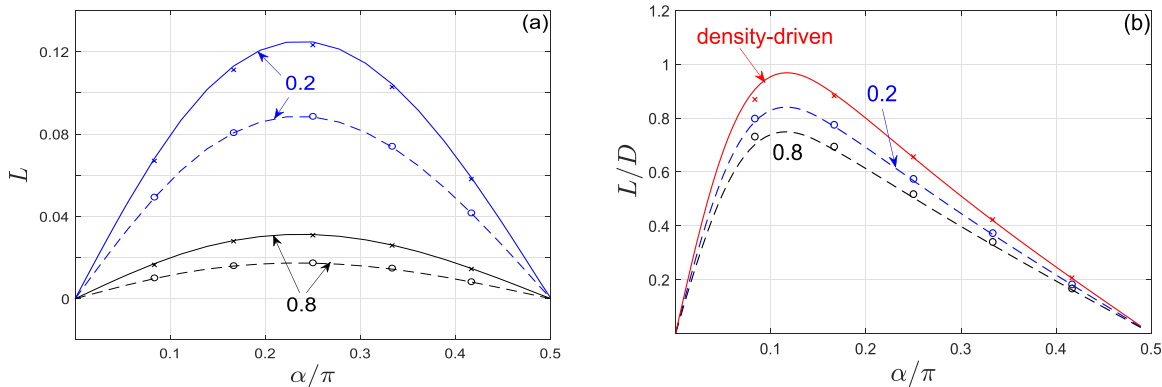
FIG. 10. Variations of the free-molecular (a) lift and (b) lift-over-drag ratio with the plate angle of attack in a diffuse-wall tunnel for density-driven (solid lines) and temperature-driven (dashed curves) flows. The numbers indicate the values of ρ_{out} (= 0.8, 0.2 with $T_{out} = 1$) or T_{out} (= 0.8, 0.2 with $\rho_{out} = 1$). The symbols denote DSMC predictions at Kn = 10 in the respective density-driven (crosses) and temperature-driven (circles) setups.

$$F_S^{(FS,diff)} = U_S \left[U_N \, \text{erf}(U_N) + \frac{1}{\sqrt{\pi}} \exp\left[-U_N^2\right] \right], \quad (25)$$

respectively. Here, $U_N = U_0 \sin\alpha, U_S = U_0 \cos\alpha$, and $\text{erf}(s) = 2\pi^{-1/2} \int_0^s \exp\left[-q^2\right] dq$ denotes the Gauss error function. In terms of F_N and F_S, the corresponding lift and drag forces are given by

$$L = F_N \cos\alpha - F_S \sin\alpha \quad \text{and} \quad D = F_N \sin\alpha + F_S \cos\alpha, \quad (26)$$

respectively.

Markedly, the problem considered in the present work corresponds to a setup that is inherently different from the free-stream description. Apart from containing the effect of sidewall reflections, we
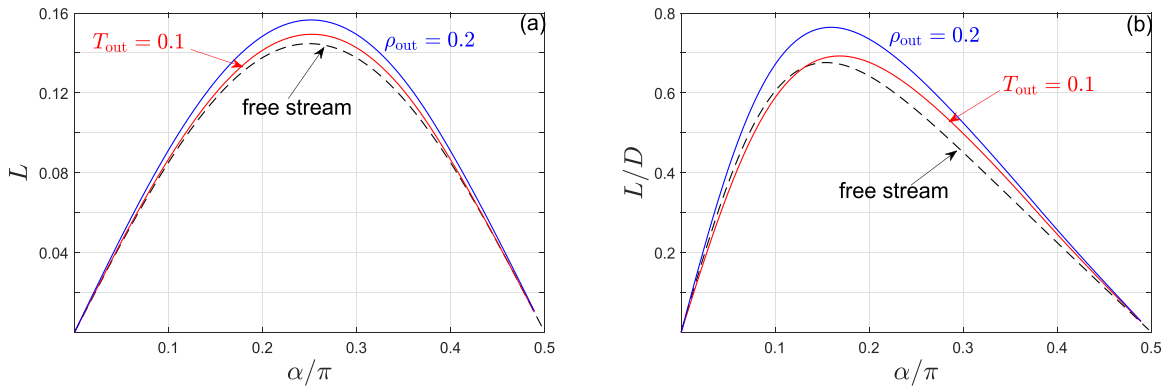
FIG. 11. Variations with plate inclination of the (a) lift force and (b) lift-to-drag ratio for collisionless free-stream flow (dashed curves) and tunnel flow (blue and red lines). The free-stream results are for a diffuse plate set at uniform x-directed flow of speed $U_0 = 0.2$. The blue and red curves mark the predictions for density-driven (with $\rho_{out} = 0.2$) and temperature-driven (with $T_{out} = 0.1$) flows in a diffuse tunnel of width $H = 10$, respectively.

consider a "blow-down" tunnel configuration, where the flow field combines Maxwellians of vanishing macroscopic velocities carried by the particles entering the tunnel inlet and outlet sections. Lacking the mitigating mechanism of molecular collisions at Kn $\gg$ 1, those zero-velocity Maxwellians characterize all particles in the domain, in both diffuse- and specular-wall configurations. While producing a non-vanishing velocity due to problem asymmetry, it may not be expected that the present hydrodynamic description converges uniformly to the free-stream limit in the case where the tunnel walls are far apart. Notably, this is different from blow-down tunnels operating at continuum flow conditions, where molecular collisions dominate the flow field and equivalence may be tabulated between the imposed inlet-to-outlet pressure ratio and free-stream flow conditions.

To inspect the similarities between the present and free-stream results, Fig. 11 shows the variations with plate inclination of the free-molecular lift force [Fig. 11(a)] and lift-to-drag ratio [Fig. 11(b)] in the free-stream description and in diffuse-tunnel setups. The dashed black lines mark the free-stream results for a diffuse plate set at x-directed uniform flow of speed $U_0 = 0.2$ [according to Eqs. (24)–(26)], whereas the solid curves present counterpart predictions in a diffuse tunnel of width $H = 10$. Specifically, the blue and red lines show results for a density-driven case with $\rho_{out} = 0.2$ and a temperature-driven configuration with $T_{out} = 0.1$, respectively. The choices for ρ_{out} and T_{out} are made such that the mean velocity magnitude at the tunnel inlet section approximately matches with the above $U_0 \approx 0.2$ in each case. In general, the gas velocity at the inlet section is not uniform, and only an average approximation can be made. In line with the discussion in Sec. V B, larger pressure gradients between the reservoirs should be imposed in the temperature-driven case (compared with the density-driven setup) to achieve a similar $U_0 \approx 0.2$ inlet speed.

While the differences between the free-stream and blow-down tunnel configurations are evident, the results in Fig. 11 indicate that the variances between the calculated aerodynamic loadings are relatively small. Both density- and temperature-driven setups yield similar non-monotonic variations of the lift and lift-to-drag ratio, with their peak locations in the latter slightly shifted to higher α compared with the free-stream result. In particular, the temperature-driven lift variation closely agrees with the free-stream curve with a deviation of less than $\approx 3\%$ at its peak value. The better correlation between the

temperature-driven (compared with the density-driven) and free-stream results may be rationalized by the more similar exponential dependence of the Maxwellian distribution on the outlet gas temperature T_{out} and the velocity U_0 [cf. Eqs. (8) and (27)], compared with its linear dependence on the outlet density ρ_{out}.

To further assess the convergence of our scheme to the free-stream limit, it is of interest to apply our computation to a case where the imposed pressure difference between the inlet and outlet reservoirs is replaced by identical Maxwellians of nonzero x-directed U_0 velocity. Specifically, the distributions in Eq. (8) are replaced by

$$f_{in} = f_{out} = \frac{1}{\pi^{3/2}} \exp\left[-|\boldsymbol{\xi} - U_0\hat{\mathbf{x}}|^2\right], \quad (27)$$

and the free-molecular scheme of solution follows similar to Sec. III. Here, the flow field combines particles characterized by U_0-drifted Maxwellians and is expected to converge to the non-confined description with increasing channel width, $H \gg 1$. The following examination should therefore provide information regarding the net impact of tunnel walls on the deviation of the boundary-confined calculation from free-stream conditions in the Kn $\gg$ 1 regime.

Figure 12 examines the convergence of the free-molecular solution in a tunnel for the lift [Fig. 12(a)] and lift-to-drag ratio [Fig. 12(b)] to the free-stream result. To compare with Fig. 11, diffuse plate and diffuse-wall tunnel setups are considered with $U_0 = 0.2$. The results for channels of widths $H = 2$, 5, and 10 are shown together with the counterpart free-stream result (identical with the dashed lines in Fig. 11). At finite channel widths, the lift force is lower than at free-stream conditions due to the loss of flow momentum by tunnel wall collisions. With increasing channel width, the results indicate the uniform convergence (at all α) of the tunnel-confined solution to the free-stream results. At $H = 10$ (where the top and bottom tunnel walls are located five chord lengths away from the chord midpoint), the sidewall effects become negligible and the tunnel-setup results become nearly identical with the free-stream limit.

Having acknowledged the differences between the U_0-velocity and blow-down problem configurations, we conclude by analyzing the large-H limit behavior of the system set in Fig. 1. In this case, the effect of tunnel top and bottom surfaces is negligible and the problem involves particles approaching the plate surface from either the left

02 May 2024 14:08:11
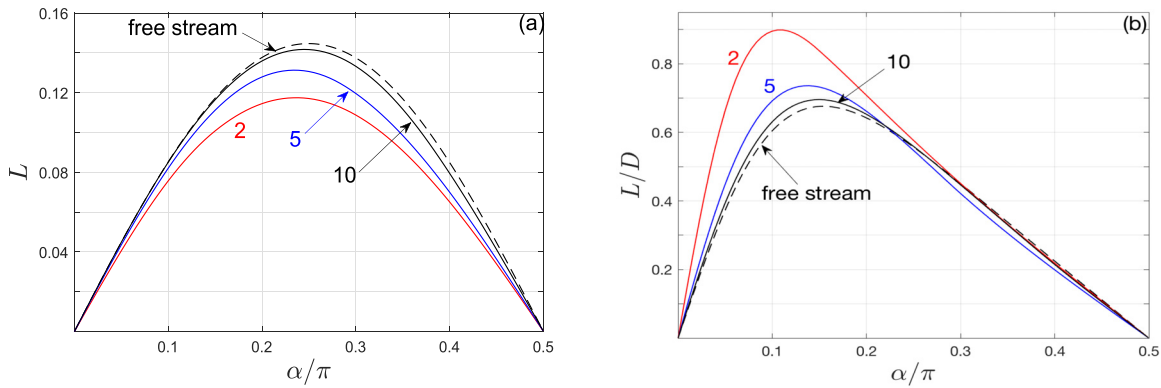
FIG. 12. Convergence of the free-molecular (a) lift force and (b) lift-to-drag ratio to the free-stream limit in a diffuse-wall tunnel with $U_0 = 0.2$. The red, blue, and black curves show variations with the plate angle of attack at the indicated $H = 2$, 5, and 10 tunnel width values, respectively. The dashed lines show the counterpart free-stream results for a diffuse reflecting plate.

(having $\xi_x > 0$ and acquiring the inlet Maxwellian distribution) or right (with $\xi_x < 0$ and outlet reservoir distribution) sides. Due to problem asymmetry, net flow is generated in the x-direction and the free-molecular loading on the plate may be computed in a closed integral form. The calculation for both specular- and diffuse-plate configurations is summarized in Appendix B.

To illustrate the results, Fig. 13(a) shows the convergence with H of the full free-molecular solution for the drag force over a specular plate for $\rho_{out} = 0.2$, $T_{out} = 1$ and the specified values of the plate angle of attack α. The limit-case values calculated in Appendix B are marked by dashed lines. It is observed that convergence is achieved for $H \gtrsim 20$, where the force becomes independent of H. In this respect, the results presented in Secs. V A and V B, for which $H = 2$, depend on H, to show the particular effect of tunnel boundaries and reflections on the flow field. Taking H to be large minimizes this impact due to the increase in geometrical decay of the signal emitted from the walls.

The results in Fig. 13(a) are complemented by reconsidering the large-H limit of the velocity reservoir system behavior. In Fig. 13(b), our data for the lift force in a diffuse-wall tunnel are shown for $U_0 = 0.2$ and the same values of α as in Fig. 13(a). As in the thermodynamic reservoir setup, it is observed that convergence is achieved for

$H \gtrsim 20$, where the free-stream force tabulated in Eqs. (24)–(26) is reached. In view of the findings in Fig. 13, we observe that the results presented in Secs. V A and V B for a relatively narrow $H = 2$ tunnel are affected by the sidewall tunnel reflections. This is in line with one of the objectives of the present work, being the of the walls' coupling effect in a rarefied gas wind tunnel.

VI. CONCLUSION

We investigated the steady aerodynamic field about a thin flat plate placed in a blow-down wind tunnel at non-continuum conditions. Considering a two-dimensional straight tunnel configuration, the flow is driven by pressure differences between the inlet and outlet tunnel sections, imposed by either density or temperature variations between the inlet and outlet gas reservoirs. Focusing on highly rarefied conditions, we derived a semi-analytic description for the gas flow field in the free-molecular limit for both diffuse- and specular-wall configurations. The solution is valid at arbitrary plate inclinations α and imposed differences between inlet and outlet reservoirs. The results were compared with direct simulation Monte Carlo calculations, indicating that the free-molecular description is valid up to $O(1)$ plate-size-based Knudsen numbers. The aerodynamic lift and
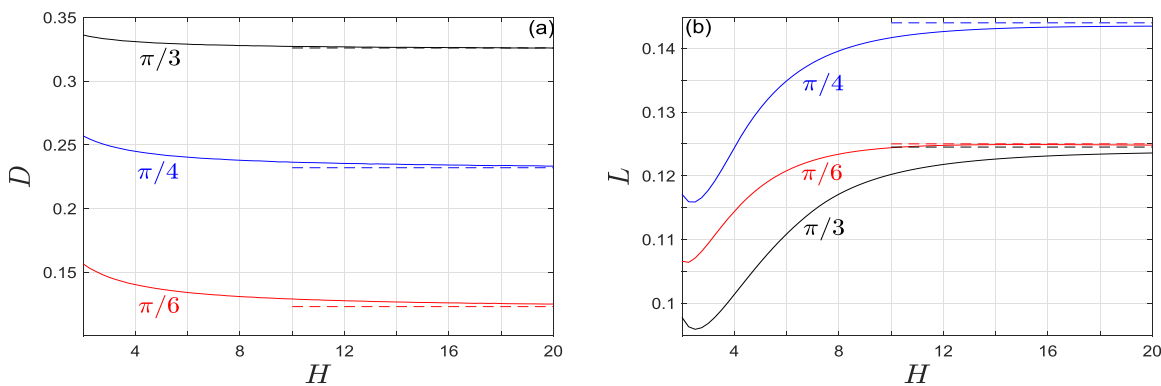
FIG. 13. Variation with H of the free-molecular (a) drag force in a specular-wall tunnel with $\rho_{out} = 0.2$, $T_{out} = 1$; (b) lift force in a diffuse-wall tunnel with $U_0 = 0.2$. The numbers indicate the values of α, the plate angle of attack, and the dashed lines mark the large-H asymptotes calculated in Appendix B for (a) and in Eqs. (24)–(26) for (b).

drag forces were evaluated and their variations with α and the outlet reservoir conditions were analyzed. While the lift-to-drag ratio decreases monotonically with α in the specular-wall setup, it reaches a maximum value in the diffuse-wall case at an intermediate value of a relatively small α. At a fixed pressure ratio between the outlet and inlet reservoirs, the density-driven setup yields higher aerodynamic loads compared with its counterpart temperature-driven configuration, in line with the associated larger mass flow rate taking place in the former. The results were discussed in light of existing rarefied-gas investigations of the non-confined (free-stream) problem. The tunnel-confined predictions for the aerodynamic loadings uniformly converge to their free-stream limit in the case where the pressure gradient is replaced by imposition of the gas velocity at the tunnel reservoirs. The results indicate that the impact of tunnel confinement at high Knudsen numbers becomes vanishingly small in the case where the tunnel walls are placed more than ≈ 10 chord-lengths away from the plate.

The present work focuses on a highly rarefied flow regime. In this case, the application of the "half-space" inlet and outlet section conditions in Eq. (1) is justified, as the interaction between outgoing and incoming particles at the tunnel open edges is negligible. In marked difference, counterpart continuum-regime formulations of wind tunnel flows impose the overall pressures at the tunnel entrance and exit, enabling the tabulation of the imposed pressure ratio vs the inlet velocity. A detailed comparison between the present high-Kn and continuum analyses is therefore obviated. However, inasmuch as ballistic free-stream plate aerodynamics deviates considerably from its counterpart continuum description, large differences are also viewed in the present tunnel flow analysis. Thus, apart from not observing flow separation at non-small angles of attack, even the seemingly linear variation of the lift force at $\alpha \ll 1$ [see Figs. 11(a) and 12(a) at small α] shows a significantly different lift curve slope. Specifically, while $\partial L/\partial \alpha = \pi/U_0^2$ according to incompressible thin-airfoil theory (equivalent to the 2π-slope in the common $\rho_{\rm in}^* U_0^{*2} c^*/2$ scaling), a much lower value of $\partial L/\partial \alpha \approx \pi^{-1}$ is viewed according to Figs. 11(a) and 12(a) for $U_0 = 0.2$ in the free-molecular limit.

Blow-down tunnels are commonly designed to operate at high-Mach flow conditions. These are achieved by adding a nozzle upstream of the tunnel inlet, through which the incoming flow is accelerated and supersonic speeds may be obtained. Since the present work focuses on a pressure-driven straight tunnel geometry, relatively low flow velocities have been considered, limited by the minimum vacuum pressure that may be imposed at the outlet reservoir (see the discussion following Fig. 8). High-speed setups may yet be studied through substitution of arbitrarily large values of U_0 in the velocity reservoir formulation introduced in Sec. V C. In this context, we consider the present work as a first step toward studying rarefied gas tunnel aerodynamics, where future investigations may examine the problem at higher flow velocities. This, together with the extension of our calculations to more complex airfoil configurations, constitute topics for future studies.

ACKNOWLEDGMENTS

AUTHOR DECLARATIONS
Conflict of Interest

The authors have no conflicts to disclose.

Author Contributions

R. Shapiro: Conceptualization (supporting); Data curation (equal); Formal analysis (lead); Investigation (equal); Validation (equal). **A. Manela:** Conceptualization (lead); Data curation (equal); Formal analysis (supporting); Funding acquisition (lead); Investigation (equal); Supervision (lead); Validation (equal); Writing – original draft (lead); Writing – review & editing (lead).

DATA AVAILABILITY

The data that support the findings of this study are available from the corresponding author upon reasonable request.

APPENDIX A: IMPERMEABILITY CONDITIONS IN A DIFFUSE-WALL TUNNEL

Following similar considerations to those described in Sec. III A for the imposition of the no-penetration condition over the tunnel upper wall, the counterpart conditions along all other solid surfaces may be derived. Skipping the technical details of calculation, the conditions are listed below.

For the lower tunnel wall, we find

$$
2\rho_{\rm lw}(x_b) - \int_{-1/2}^{1/2} \rho_{\rm lp}(z) \frac{(z\sin\alpha - H/2)(x_b\sin\alpha - (H\cos\alpha)/2)}{\left[(z\sin\alpha - H/2)^2 + (x_b - z\cos\alpha)^2\right]^{3/2}}\, dz
$$
$$
- H^2 \int^{\rm uw} \frac{\rho_{\rm uw}(x)dx}{\left[H^2 + (x - x_b)^2\right]^{3/2}} = -\left[\frac{L/2 + x_b}{\sqrt{H^2 + (L/2 + x_b)^2}} - 1\right]
$$
$$
- \rho_{\rm out}\sqrt{T_{\rm out}}\left[\frac{L/2 - x_b}{\sqrt{H^2 + (L/2 - x_b)^2}} - 1\right], \tag{A1}
$$

balancing the contributions of reflected lower-wall and incoming bottom plate and upper wall particles on the left-hand side, with the forcing inlet and outlet section terms on the right-hand side. Similar to Eq. (16) [see Eq. (13) *et seq.*], in cases where the lower surface of the plate is obscured and particles arrive from the plate upper wall, $\rho_{\rm lp}(z)$ in Eq. (A1) is replaced by $\rho_{\rm up}(z)$. In addition, the $\rho_{\rm uw}(x)$ integral is carried out over the $x_{\rm uw}$ portion of the upper wall that transmits particles to x_b [cf. the discussion of x_l and x_r in the context of Eq. (12)]. The above equation is formulated for a case where particles may arrive at x_b from any point along the inlet and outlet sections. Configurations where these sections are partly obscured by the airfoil are not detailed here, but may be retrieved based on elementary geometrical considerations.

Over the plate lower side, we obtain

$$
2\rho_{\rm lp}(x_b) - \int^{\rm uw} \rho_{\rm uw}(x) \frac{(x\sin\alpha + H/2)(x_b\sin\alpha + (H\cos\alpha)/2)}{\left[(x\sin\alpha + H/2)^2 + (x_b - x\cos\alpha)^2\right]^{3/2}}\, dx
$$
$$
- \int^{\rm lw} \rho_{\rm lw}(x) \frac{(H/2 - x\sin\alpha)[(H\cos\alpha)/2 - x_b\sin\alpha]}{\left[(H/2 - x\sin\alpha)^2 + (x\cos\alpha - x_b)^2\right]^{3/2}}\, dx
$$

$$= 2 \int_0^\infty \xi_y \left[\mathrm{erf}(-a_{\mathrm{in}}\xi_y) - \mathrm{erf}(-b_{\mathrm{in}}\xi_y) \right] \exp\left[-\xi_y^2\right] \mathrm{d}\xi_y$$

$$+ \frac{2\rho_{\mathrm{out}}}{\sqrt{T_{\mathrm{out}}}} \int_0^\infty \xi_y \left[\mathrm{erf}\left(-\frac{a_{\mathrm{out}}\xi_y}{\sqrt{T_{\mathrm{out}}}}\right) - \mathrm{erf}\left(-\frac{b_{\mathrm{out}}\xi_y}{\sqrt{T_{\mathrm{out}}}}\right) \right]$$

$$\times \exp\left[-\frac{1}{T_{\mathrm{out}}}\xi_y^2\right]\mathrm{d}\xi_y, \tag{A2}$$

where the $\rho_{\mathrm{uw}}(x)$ and $\rho_{\mathrm{lw}}(x)$ integrals are carried out over the x_{uw} and x_{lw} portions of the upper and lower walls, respectively, that transmit particles to x_b. On the right-hand side, $\mathrm{erf}(s) = 2\pi^{-1/2} \int_0^s \exp\left[-q^2\right]\mathrm{d}q$ marks the Gauss error function. Additionally, $a_{\mathrm{in/out}}$ and $b_{\mathrm{in/out}}$ reflect the partial integration over ξ_x in the inlet/outlet section contributions that may be partly obscured. Similarly, over the plate upper surface we get

$$2\rho_{\mathrm{up}}(x_b) - \int^{\mathrm{uw}} \rho_{\mathrm{uw}}(x) \frac{(x\sin\alpha + H/2)(x_b\sin\alpha + (H\cos\alpha)/2)}{\left[(x\sin\alpha + H/2)^2 + (x_b - x\cos\alpha)^2\right]^{3/2}}\mathrm{d}x$$

$$- \int^{\mathrm{lw}} \rho_{\mathrm{lw}}(x) \frac{(H/2 - x\sin\alpha)[(H\cos\alpha)/2 - x_b\sin\alpha]}{\left[(H/2 - x\sin\alpha)^2 + (x\cos\alpha - x_b)^2\right]^{3/2}}\mathrm{d}x$$

$$= 2 \int_{-\infty}^0 \xi_y \left[\mathrm{erf}(-a_{\mathrm{in}}\xi_y) - \mathrm{erf}(-b_{\mathrm{in}}\xi_y) \right] \exp\left[-\xi_y^2\right] \mathrm{d}\xi_y$$

$$+ \frac{2\rho_{\mathrm{out}}}{\sqrt{T_{\mathrm{out}}}} \int_{-\infty}^0 \xi_y \left[\mathrm{erf}\left(-\frac{a_{\mathrm{out}}\xi_y}{\sqrt{T_{\mathrm{out}}}}\right) - \mathrm{erf}\left(-\frac{b_{\mathrm{out}}\xi_y}{\sqrt{T_{\mathrm{out}}}}\right) \right]$$

$$\times \exp\left[-\frac{1}{T_{\mathrm{out}}}\xi_y^2\right]\mathrm{d}\xi_y. \tag{A3}$$

APPENDIX B: PLATE LOADING IN THE FREE-MOLECULAR LARGE-H LIMIT

Considering the non-dimensional counterpart of the system in Fig. 1 and omitting the effect of tunnel upper and lower surfaces, particles approaching the plate surface acquire either the inlet ($f_{\mathrm{in}} = \pi^{-3/2} \exp[-\xi^2]$) or outlet ($f_{\mathrm{out}} = (\pi T_{\mathrm{out}})^{-3/2}\rho_{\mathrm{out}} \exp[-\xi^2/T_{\mathrm{out}}]$) reservoir distributions. In this case, the expressions for the force on the plate may be formulated in an integral form, as detailed below for diffuse- (Sec. 1 of Appendix B) and specular- (Sec. 2 of Appendix B) plate setups. The calculation constitutes a particular case of the tunnel-flow analysis presented in Sec. III with the effect of upper and lower wall reflections removed.

1. Diffuse plate

Following the procedure described in Sec. III A, the free-stream equations for the impermeability condition over the plate upper and lower surfaces may be solved in a closed form, yielding

$$\rho_{\mathrm{up}} = \frac{1 + \rho_{\mathrm{out}}\sqrt{T_{\mathrm{out}}}}{2} + \int_0^\infty s\,\mathrm{erf}(s\tan\alpha)\exp[-s^2]\mathrm{d}s$$

$$- \left(\rho_{\mathrm{out}}/\sqrt{T_{\mathrm{out}}}\right)\int_0^\infty s\,\mathrm{erf}\left(s\tan\alpha/\sqrt{T_{\mathrm{out}}}\right)\exp\left[-s^2/T_{\mathrm{out}}\right]\mathrm{d}s \tag{B1}$$

and

$$\rho_{\mathrm{lp}} = \frac{1 + \rho_{\mathrm{out}}\sqrt{T_{\mathrm{out}}}}{2} - \int_{-\infty}^0 s\,\mathrm{erf}(s\tan\alpha)\exp[-s^2]\mathrm{d}s$$

$$+ \left(\rho_{\mathrm{out}}/\sqrt{T_{\mathrm{out}}}\right)\int_{-\infty}^0 s\,\mathrm{erf}\left(s\tan\alpha/\sqrt{T_{\mathrm{out}}}\right)\exp\left[-s^2/T_{\mathrm{out}}\right]\mathrm{d}s. \tag{B2}$$

The expressions for the lift and drag forces over the plate follow using Eqs. (20) and (21), respectively. To this end, we make use of Eq. (18) after replacing all x and y indices by $s_\parallel$ and $s_\perp$, respectively, and apply the impermeability condition ($u_{s_\perp} = 0$ over the plate wall). This yields, for the normal stress over the upper plate surface

$$P_{s_\perp s_\perp}(-0.5 \le s_\parallel \le 0.5, s_\perp = 0^+)$$

$$= \frac{\rho_{\mathrm{up}}}{4} + \frac{1 + \rho_{\mathrm{out}}T_{\mathrm{out}}}{8} + \frac{1}{2\sqrt{\pi}}\int_{-\infty}^0 s^2 \mathrm{erf}(s\tan\alpha)\exp[-s^2]\mathrm{d}s$$

$$- \frac{\rho_{\mathrm{out}}}{2\sqrt{\pi T_{\mathrm{out}}}}\int_{-\infty}^0 s^2 \mathrm{erf}\left(s\tan\alpha/\sqrt{T_{\mathrm{out}}}\right)\exp\left[-s^2/T_{\mathrm{out}}\right]\mathrm{d}s \tag{B3}$$

and over the lower plate surface

$$P_{s_\perp s_\perp}(-0.5 \le s_\parallel \le 0.5, s_\perp = 0^-)$$

$$= \frac{\rho_{\mathrm{lp}}}{4} + \frac{1 + \rho_{\mathrm{out}}T_{\mathrm{out}}}{8} + \frac{1}{2\sqrt{\pi}}\int_0^\infty s^2 \mathrm{erf}(s\tan\alpha)\exp[-s^2]\mathrm{d}s$$

$$- \frac{\rho_{\mathrm{out}}}{2\sqrt{\pi T_{\mathrm{out}}}}\int_0^\infty s^2 \mathrm{erf}\left(s\tan\alpha/\sqrt{T_{\mathrm{out}}}\right)\exp\left[-s^2/T_{\mathrm{out}}\right]\mathrm{d}s. \tag{B4}$$

For the shear stress over the upper surface, we find

$$P_{s_\parallel s_\perp}(-0.5 \le s_\parallel \le 0.5, s_\perp = 0^+) = \frac{\rho_{\mathrm{out}}T_{\mathrm{out}} - 1}{4\pi(1 + \tan^2\alpha)} \tag{B5}$$

and over the lower surface $P_{s_\parallel s_\perp}(s_\perp = 0^-) = -P_{s_\parallel s_\perp}(s_\perp = 0^+)$. The quadratures required for calculating the lift and drag forces in Eqs. (20) and (21) are straightforward since the expressions for all stress components are independent of $s_\parallel$.

2. Specular plate

For convenience, the calculation in the specular-plate setup is carried out in the (x, y) system of coordinates [rather than $(s_\parallel, s_\perp)$], to express P_{xx}, P_{yy}, and P_{xy} over the plate surface. To simplify presentation, we provide below expressions for the required fields over the upper plate surface only ($s_\perp = 0^+$). Counterpart expressions over the lower plate boundary follow by symmetry.

In line with Eq. (18), we put

$$P_{xx} = \int_{-\infty}^\infty (\xi_x - u_x)^2 f\mathrm{d}\boldsymbol{\xi} = I_{xx} - \rho u_x^2,$$

$$P_{yy} = \int_{-\infty}^\infty (\xi_y - u_y)^2 f\mathrm{d}\boldsymbol{\xi} = I_{yy} - \rho u_y^2 \tag{B6}$$

and $\quad P_{xy} = \int_{-\infty}^\infty (\xi_x - u_x)(\xi_y - u_y)f\mathrm{d}\boldsymbol{\xi} = I_{xy} - \rho u_x u_y.$

Below, we provide expressions for the density ρ, velocity components u_x and u_y, and integral fields I_{xx}, I_{yy}, and I_{xy}, appearing in Eq. (B6), based on Eqs. (17) and (18). Starting with the density over the upper plate surface, we find

$$\rho(-0.5 \le s_\parallel \le 0.5, s_\perp = 0^+)$$

$$= \frac{1 + 3\rho_{\text{out}}}{4} + \frac{1}{2\sqrt{\pi}} \int_0^\infty \text{erf}\left(\frac{\xi_x}{\tan 2\alpha}\right) \exp\left[-\xi_x^2\right] \mathrm{d}\xi_x$$

$$- \frac{\rho_{\text{out}}}{2\sqrt{\pi T_{\text{out}}}} \int_0^\infty \text{erf}\left(\frac{\xi_x}{\sqrt{T_{\text{out}}}\tan 2\alpha}\right) \exp\left[-\xi_x^2/T_{\text{out}}\right] \mathrm{d}\xi_x. \quad \text{(B7)}$$

Proceeding to the x- and y-velocity components, we obtain

$$u_x(-0.5 \le s_\parallel \le 0.5, s_\perp = 0^+)$$

$$= \frac{1}{\rho}\left[\frac{1 - \rho_{\text{out}}\sqrt{T_{\text{out}}}}{4\sqrt{\pi}} + \frac{1}{2\sqrt{\pi}} \int_0^\infty \xi_x \text{erf}\left(\frac{\xi_x}{\tan 2\alpha}\right) \exp\left[-\xi_x^2\right] \mathrm{d}\xi_x\right.$$

$$\left. - \frac{\rho_{\text{out}}}{2\sqrt{\pi T_{\text{out}}}} \int_0^\infty \xi_x \text{erf}\left(\frac{\xi_x}{\sqrt{T_{\text{out}}}\tan 2\alpha}\right) \exp\left[-\xi_x^2/T_{\text{out}}\right] \mathrm{d}\xi_x\right]$$

$$\text{(B8)}$$

and

$$u_y(-0.5 \le s_\parallel \le 0.5, s_\perp = 0^+) = \frac{\sin 2\alpha(\rho_{\text{out}}\sqrt{T_{\text{out}}} - 1)}{4\rho\sqrt{\pi}}. \quad \text{(B9)}$$

For I_{xx}, I_{yy}, and I_{xy}, we compute

$$I_{xx}(-0.5 \le s_\parallel \le 0.5, s_\perp = 0^+)$$

$$= \frac{1 - \rho_{\text{out}}T_{\text{out}}}{8} + \frac{1}{2\sqrt{\pi}} \int_0^\infty \xi_x^2 \text{erf}\left(\frac{\xi_x}{\tan 2\alpha}\right) \exp\left[-\xi_x^2\right] \mathrm{d}\xi_x$$

$$- \frac{\rho_{\text{out}}}{2\sqrt{\pi T_{\text{out}}}} \int_0^\infty \xi_x^2 \text{erf}\left(\frac{\xi_x}{\sqrt{T_{\text{out}}}\tan 2\alpha}\right) \exp\left[-\xi_x^2/T_{\text{out}}\right] \mathrm{d}\xi_x,$$

$$\text{(B10)}$$

$$I_{yy}(-0.5 \le s_\parallel \le 0.5, s_\perp = 0^+)$$

$$= \frac{\pi(1 + 3\rho_{\text{out}}) + \sin 2\alpha(\rho_{\text{out}}T_{\text{out}} - 1)}{8\pi}$$

$$+ \frac{1}{4\sqrt{\pi}} \int_0^\infty \text{erf}\left(\frac{\xi_x}{\tan 2\alpha}\right) \exp\left[-\xi_x^2\right] \mathrm{d}\xi_x$$

$$- \frac{\rho_{\text{out}}\sqrt{T_{\text{out}}}}{4\sqrt{\pi}} \int_0^\infty \text{erf}\left(\frac{\xi_x}{\sqrt{T_{\text{out}}}\tan 2\alpha}\right) \exp\left[-\xi_x^2/T_{\text{out}}\right] \mathrm{d}\xi_x,$$

$$\text{(B11)}$$

and

$$I_{xy}(-0.5 \le s_\parallel \le 0.5, s_\perp = 0^+) = \frac{(\rho_{\text{out}}T_{\text{out}} - 1)\sin^2 2\alpha}{4\pi}. \quad \text{(B12)}$$

Substituting Eqs. (B7)–(B12) into Eq. (B6), we obtain P_{xx}, P_{yy}, and P_{xy} over the plate upper surface. Subsequently, $P_{s_\perp s_\perp}(s_\perp = 0^+)$ and $P_{s_\parallel s_\perp}(s_\perp = 0^+)$ [as well as their counterparts over the lower $s_\perp = 0^-$ surface, following symmetry considerations] are calculated through standard projections of the x- and y-directions over $s_\parallel$ and $s_\perp$. The expressions for the lift and drag forces over the specular plate are then derived following Eqs. (20) and (21).

REFERENCES

[1] H. Glauert, *Wind Tunnel Interference on Wings, Bodies and Airscrews* (H.M. Stationery Office, London, 1933).

[2] X.-Y. Sun, T.-E. Li, G.-C. Lin, and Y. Wu, "A study on the aerodynamic characteristics of a stratospheric airship in its entire flight envelope," Proc. Inst. Mech. Eng., Part G **232**, 902–921 (2018).

[3] Z. Zuo, J. Song, Z. Zheng, and Q.-L. Han, "A survey on modelling, control and challenges of stratospheric airships," Control Eng. Pract. **119**, 104979 (2022).

[4] M. Cimini, M. Pizzarelli, and M. Bernardini, "Aerothermodynamic analysis of high-altitude space launcher with direct-simulation Monte Carlo method," AIAA J. **57**, 2534–2543 (2019).

[5] G. Zuppardi and G. Mongelluzzo, "Aerodynamics of a wing section along an entry path in Mars atmosphere," Adv. Aircr. Spacecr. Sci. **8**, 53–67 (2021).

[6] G. Zuppardi and G. Mongelluzzo, "Aerodynamics of a concept space plane in high-altitude earth reentry," J. Spacecr. Rockets **60**, 361–365 (2023).

[7] B. Liu, X. L. Yang, J. Yang, and G. Gao, "Recent advances in MEMS-based microthrusters," Micromachines **10**, 818 (2019).

[8] N. Myakishev, M. Laptev, A. Pekarskii, V. Barskov, V. Rassokhin, V. Chernikov, E. Semakina, V. Yadikin, Y. Matveev, and A. Smetankin, "Review of the current state of research of microturbine units," IOP Conf. Ser.: Mater. Sci. Eng. **986**, 012061 (2020).

[9] J. Xu, J. Zhang, F. Li, S. Liu, Y. Ye, and R. Shen, "A review on solid propellant micro-thruster array based on MEMS technology," FirePhysChem (published online, 2023).

[10] A. Ball, J. Garry, R. Lorenz, and V. Kerzhanovich, *Planetary Landers and Entry Probes* (Cambridge University Press, Cambridge, 2009).

[11] M. Guelman, "Closed-loop control of close orbits around asteroids," J. Guid., Control Dyn. **38**, 854–860 (2015).

[12] J. Allegre, "The SR3 low density wind tunnel—Facility capabilities and research development," AIAA Paper No. 92-3972, 1992.

[13] J. Gumbel, M. Khaplanov, C. Unckell, and M. Rapp, "Wind tunnel studies and simulations of rarefied aerodynamics," in *Proceedings of the 14th ESA Symposium on European Rocket and Balloon Programs and Related Research* (ESA, 1999), pp. 471–476.

[14] T. Ozawa, T. Suzuki, and K. Fujita, "Rarefied aerodynamic measurements in hypersonic rarefied wind tunnel," AIP Conf. Proc. **1628**, 1284 (2014).

[15] E. Kustova, A. Krylov, V. Lashkov, and M. Mekhonoshina, "Experimental facilities and modelling for rarefied aerodynamics," Report No. EN-AVT-194-13 (North Atlantic Treaty Organization Science and Technology, 2011).

[16] N. Rembaut, R. Joussot, and V. Lago, "Aerodynamical behavior of spherical debris in the supersonic and rarefied wind tunnel MARHy," J. Space Saf. Eng. **7**, 411–419 (2020).

[17] J. R. Stadler and V. J. Zurick, "Theoretical aerodynamic characteristics of bodies in a free-molecular-flow field," NACA Report No. 2423, 1951.

[18] C. Cercignani and M. Lampis, "Free molecular flow past a flat plate in the presence of a nontrivial gas-surface interaction," J. Appl. Math. Phys. **23**, 713–728 (1972).

[19] K. Aoki, K. Kanba, and S. Takata, "Numerical analysis of a supersonic rarefied gas flow past a flat plate at an angle of attack," Phys. Fluids **9**, 1144–1161 (1997).

[20] Q. Sun, I. D. Boyd, and G. Candler, "Numerical simulation of gas flow over microscale airfoils," J. Thermophys. Heat Transfer **16**, 171–179 (2002).

[21] Q. Sun and I. D. Boyd, "Drag on a flat plate in low-Reynolds-number gas flows," AIAA J. **42**, 1066–1072 (2004).

[22] Q. Sun and I. D. Boyd, "Flat-plate aerodynamics at very low Reynolds number," J. Fluid Mech. **502**, 199–206 (2004).

[23] A. A. Abramov, A. V. Butkovskii, and O. Buzykin, "Rarefied gas flow past a flat plate at zero angle of attack," Phys. Fluids **32**, 087108 (2020).

[24] J. Fan, I. D. Boyd, and C.-P. Cai, "Computation of rarefied gas flows around a NACA 0012 airfoil," AIAA J. **39**, 618–625 (2001).

[25] A. Shoja-Sani, E. Roohi, M. Kahroma, and S. Stefanov, "Investigation of aerodynamic characteristics of rarefied flow around NACA 0012 airfoil using DSMC and NS solvers," Eur. J. Mech. B **48**, 59–74 (2014).

[26] C. Pekardan and A. Alexeenko, "Rarefaction effects for transonic airfoil flows at low Reynolds numbers," AIAA J. **56**, 765–779 (2018).

[27] S. Pantazis, D. Valougeorgis, and F. Sharipov, "End corrections for rarefied gas flows through capillaries of finite length," Vacuum **97**, 26–29 (2013).

[28] Y. Sone, *Molecular Gas Dynamics: Theory, Techniques, and Applications* (Birkhäuser, Boston, 2007).

[29] M. N. Kogan, *Rarefied Gas Dynamics* (Plenum, New York, 1969).

[30] G. Bird, *Molecular Gas Dynamics and the Direct Simulation of Gas Flows* (Clarendon, Oxford, 1994).

[31] W. Wagner, "A convergence proof for Bird's direct simulation Monte Carlo method for the Boltzmann equation," J. Stat. Phys. **66**, 1011–1044 (1992).

[32] IN. Ivchenko, S. K. Loyalka, and R. V. Tompson, *Analytical Methods for Problems of Molecular Transport* (Springer, The Netherlands, 2007).

[33] A. Manela and L. Gibelli, "Free-molecular and near-free-molecular gas flows over backward facing steps," J. Fluid Mech. **889**, A22 (2020).

[34] The convergence of the (practically non-physical) $T_{out} \rightarrow 0$ limit to the expansion-to-vacuum ($\rho_{out} = 0$) result is expected, since in both scenarios no particles enter the tunnel through its outlet.